Non-normality and classification of amplification mechanisms in stability and resolvent analysis

Sean Symon,* Kevin Rosenberg, Scott T. M. Dawson, and Beverley J. McKeon
Graduate Aerospace Laboratories, California Institute of Technology, Pasadena, California 91125, USA

(Received 14 December 2017; published 16 May 2018)

Eigenspectra and pseudospectra of the mean-linearized Navier-Stokes operator are used to characterize amplification mechanisms in laminar and turbulent flows in which linear mechanisms are important. Success of mean flow (linear) stability analysis for a particular frequency is shown to depend on whether two scalar measures of non-normality agree: (1) the product between the resolvent norm and the distance from the imaginary axis to the closest eigenvalue and (2) the inverse of the inner product between the most amplified resolvent forcing and response modes. If they agree, the resolvent operator can be rewritten in its dyadic representation to reveal that the adjoint and forward stability modes are proportional to the forcing and response resolvent modes at that frequency. Hence the real parts of the eigenvalues are important since they are responsible for resonant amplification and the resolvent operator is low rank when the eigenvalues are sufficiently separated in the spectrum. If the amplification is pseudoresonant, then resolvent analysis is more suitable to understand the origin of observed flow structures. Two test cases are studied: low Reynolds number cylinder flow and turbulent channel flow. The first deals mainly with resonant mechanisms, hence the success of both classical and mean stability analysis with respect to predicting the critical Reynolds number and global frequency of the saturated flow. Both scalar measures of non-normality agree for the base and mean flows, and the region where the forcing and response modes overlap scales with the length of the recirculation bubble. In the case of turbulent channel flow, structures result from both resonant and pseudoresonant mechanisms, suggesting that both are necessary elements to sustain turbulence. Mean shear is exploited most efficiently by stationary disturbances while bounds on the pseudospectra illustrate how pseudoresonance is responsible for the most amplified disturbances at spatial wavenumbers and temporal frequencies corresponding to well-known turbulent structures. Some implications for flow control are discussed.

DOI: 10.1103/PhysRevFluids.3.053902

I. INTRODUCTION

A. Background

Decomposing unsteady and turbulent flows into low-rank models is an important step towards the realization of closed-loop flow control, which has proven to be elusive (at least in part) due to the high degrees of freedom in most flow systems. Despite the inherent complexity, a time-averaged flow, or mean, that is statistically stationary can often be defined and leveraged using the eigenvalue spectrum of the governing Navier-Stokes equations (NSEs) to educe the frequencies, i.e., the imaginary part of the eigenvalues, and shapes of coherent structures which appear in the flow. Recent studies have demonstrated the success of mean flow stability analysis for a variety of flows including thermosolutal convection [1], turbulent jets [2–4], and flow over a backward-facing step

*ssymon@caltech.edu

[5]. There is also a significant body of work discussing stability analysis of the mean cylinder wake which was shown by Barkley [6] to correctly identify the frequency of the globally unstable flow above the critical Reynolds number of $\mathrm{Re} = 47$ [7–9]. Notably, classical linear stability analysis of the base flow, which is an equilibrium solution of the NSEs, at supercritical Reynolds numbers does not predict the correct observed frequency. The base (laminar) and mean (time average of the fluctuating velocity field) profiles are differentiated because of the importance of nonlinearity in sustaining the latter.

Recent work has endeavored to explain why and when mean stability analysis is valid. Barkley [6] suggested that success corresponds to cases where the Reynolds stresses are unperturbed at order ϵ when considering infinitesimal perturbations $\epsilon\tilde{\boldsymbol{u}}(x,y)\exp(\lambda t)$ to the mean flow solution. This was confirmed by Sipp and Lebedev [10], who determined that the nonlinear interaction of the leading global mode with its conjugate, i.e., the contribution to the mean Reynolds stresses, significantly outweighed the interaction of the mode with itself leading to higher frequency harmonics. As shown by Mantič-Lugo *et al.* [11] the Reynolds stresses can be approximated with the leading global mode and its conjugate. Sipp and Lebedev [10] used open cavity flow as a counterexample to the validity of mean stability analysis where the predicted frequencies do not match direct numerical simulation (DNS) of the flow. This discrepancy can be attributed to the non-normality of the flow which leads to nonorthogonality of the global modes and sensitivity of the spectrum to perturbation of the operator [12]. The behavior of these systems can be more accurately characterized by the pseudospectrum of the linearized Navier-Stokes (LNS) operator using resolvent analysis (e.g., [12,13]) rather than the spectrum alone. Jovanović and Bamieh [14] formulated the linearized problem for laminar channel flow in input-output terms, where the resolvent operator constitutes the transfer function between them, considering the componentwise transfer from harmonic exogenous disturbance or forcing (input) to velocity response (output). There is also a broad literature considering stochastic forcing (e.g., [15]), and the initial condition, transient growth problem (e.g., [16]).

McKeon and Sharma [17] and Hwang and Cossu [18] considered the resolvent reformulated with respect to the turbulent mean flow for canonical turbulent wall flows. The latter authors employed an eddy viscosity to account for the action of the Reynolds stresses, while the former analysis extends the approach to include the nonlinear terms as the input forcing to the linear operator, i.e., closing the feedback loop. McKeon and Sharma [17] performed a singular value decomposition of the resolvent to identify the inputs giving rise to the most amplified responses which are ranked by their gain (singular value). The approach has been extended to nonparallel flows (e.g., [5,19–21]). Beneddine *et al.* [5] concluded that mean stability analysis was valid when the dominant singular value of the resolvent operator was significantly greater than the others at a given frequency and that this condition holds for flows where there is a dominant convective instability mechanism and an eigenvalue which is nearly marginally stable. In such circumstances, it was shown that the eigenmodes are proportional to the resolvent response modes.

B. Motivation and scope of the study

This study addresses both stability and resolvent analyses for base and mean flows with an emphasis on the latter. The analyses are formally related through a dyad expansion of the resolvent operator and we examine the circumstances under which the stability and resolvent modes are proportional. The real part of an eigenvalue, which is difficult to interpret when the NSEs are linearized around the mean flow, is shown to be important as it influences the degree to which a disturbance is amplified. It also has a bearing on whether or not the resolvent operator is low rank since an eigenvalue must be sufficiently separated from the rest of the spectrum in order to dominate the contribution of other eigenvalues in the dyad expansion. When an eigenvalue is marginally stable, or very close to the imaginary axis, it drowns out the effect of other eigenvalues over a large range of temporal frequencies. Non-normality also plays a role in amplification and can be investigated through the lens of the pseudospectrum of the LNS operator. Most previous studies have only investigated the

pseudospectra of parallel base flows (e.g., [12,13,22–25]). In this study, pseudospectral analysis is extended to mean flows with or without streamwise development.

We compare two scalar measures of non-normality and argue that the equivalence of the two implies a resonant amplification mechanism which can be identified by mean stability analysis. The first compares the contribution from resonance, by computing the distance between the imaginary axis and the nearest eigenvalue, to the resolvent norm. The product of these two quantities is a scalar measure of non-normality. The second, which was proposed by Chomaz [26], is to calculate the inverse inner product between the most amplified resolvent forcing and response mode; this has also been applied in passing by Qadri and Schmid [27]. When these two measures agree, the most amplified structure is an eigenvector of the LNS operator. When they do not agree, amplification can be attributed to pseudoresonance. The final objective of this study is to be able to predict the type of amplification mechanism and hence the mode shapes based on the mean profile or wavenumber vector selected. Analysis of the spectra and pseudospectra of the flows considered here will form a basis for how to interpret the mechanisms identified by the resolvent for more complex flows.

C. Choice of flows and outline of the paper

We consider low Reynolds number cylinder flow and turbulent channel flow to demonstrate the contributions of this paper. Flow around a circular cylinder is an example of an oscillator flow [28] which has intrinsic dynamics that are insensitive to background noise. The flow exhibits a region of absolute instability [29,30] which can be approximated using the wavemaker (e.g., [31]). Using resolvent analysis and plotting bounds of the pseudospectrum for a given perturbation magnitude, it is evident that resonance accounts for the bulk of the amplification. The impact of mean flow advection, however, leads to a resolvent norm which is appreciably larger than the contribution from resonance alone. In the case of turbulent channel flow, which is a noise amplifier [28], the choice of temporal frequency and spatial wavenumbers has an impact on the influence of non-normality. We analyze several structures which are either highly amplified or representative of known turbulent structures in order to establish the role of resonant and pseudoresonant mechanisms as well as generalize when low-rank behavior can be expected. We stress that we consider here flows in which the dynamics of the linear operator contain features which are related to the full flow.

The rest of the paper is organized as follows. In Sec. II, the governing equations are derived for the linear operators which form the basis of stability and resolvent analyses and we review known amplification mechanisms. In Sec. III, the resolvent operator is rewritten using its dyadic representation to formally relate stability and resolvent modes and show when the rank-1 approximation is appropriate for resonant mechanisms. In this section, we introduce the scalar measures of non-normality and explore the projection of resolvent modes onto eigenmodes. Application of the findings to circular cylinder flow is considered in Sec. IV. Resolvent analysis is applied to both base and mean flows and the results are compared to those from a stability analysis. Section V considers turbulent channel flow where the influence of the wall-normal height and spatial and temporal wavenumbers are shown to play a major role in the type of amplification mechanisms which dominate as well as whether or not the resolvent is low rank. Conclusions are presented in Sec. VI along with the implications for reduced-order modeling and control.

II. REVIEW OF GOVERNING EQUATIONS AND AMPLIFICATION MECHANISMS

The relevant operators for the analyses that follow are derived from the incompressible NSEs which are nondimensionalized by the characteristic length and velocity scales, L and U:

$$\partial_t \boldsymbol{u} + \boldsymbol{u} \cdot \nabla \boldsymbol{u} = -\nabla p + \mathrm{Re}^{-1} \nabla^2 \boldsymbol{u}, \tag{1a}$$

$$\nabla \cdot \boldsymbol{u} = 0. \tag{1b}$$

The states $\boldsymbol{u}(\boldsymbol{x},t)$ and $p(\boldsymbol{x},t)$ are the spatially and temporally varying velocity and pressure fields, respectively (explicit statement of the spatial and temporal dependencies are dropped from here on for conciseness), while Re is the Reynolds number based on L and U. After Reynolds-decomposing the states into a stationary temporal mean (denoted by an overline) and a fluctuating component (denoted by a prime), one obtains the mean flow equations:

$$\overline{\boldsymbol{u}} \cdot \nabla \overline{\boldsymbol{u}} + \nabla \overline{p} - \mathrm{Re}^{-1} \nabla^2 \overline{\boldsymbol{u}} = -\overline{\boldsymbol{u}' \cdot \nabla \boldsymbol{u}'}, \tag{2a}$$

$$\nabla \cdot \overline{\boldsymbol{u}} = 0. \tag{2b}$$

For an exact solution of the NSEs, i.e., a true *base flow*, the divergence of the Reynolds stress tensor, or the right-hand term in Eq. (2a), is zero. Henceforth, we identify the temporal mean in such a case by $\overline{\boldsymbol{u}} = \boldsymbol{U}_0$. If the term is nonzero, however, $\overline{\boldsymbol{u}}$ does not constitute an exact solution and the action of Reynolds stresses must be taken into account to satisfy the NSEs. We refer to $\overline{\boldsymbol{u}}$ in this case as a (turbulent) *mean flow*.

Subtracting the mean momentum equations [Eqs. (2)] from the NSEs [Eq. (1)] yields the following for the fluctuating quantities:

$$\partial_t \boldsymbol{u}' + \overline{\boldsymbol{u}} \cdot \nabla \boldsymbol{u}' + \boldsymbol{u}' \cdot \nabla \overline{\boldsymbol{u}} + \nabla p' - \mathrm{Re}^{-1} \nabla^2 \boldsymbol{u}' = -\boldsymbol{u}' \cdot \nabla \boldsymbol{u}' + \overline{\boldsymbol{u}' \cdot \nabla \boldsymbol{u}'} = \boldsymbol{f}', \tag{3a}$$

$$\nabla \cdot \boldsymbol{u}' = 0. \tag{3b}$$

Equation (3a) has been written such that all linear terms appear on the left-hand side. The nonlinear terms on the right-hand side can be lumped together as a forcing $\boldsymbol{f}'$ without loss of generality. The literature devoted to analyzing these linearized equations is broad and covers a range of flows. We recap here the analyses required for the subsequent development and refer the reader to recent reviews and contributions [24–26,32,33] for further information.

Our development considers global and spatially periodic modes in the context of bluff body and wall-bounded turbulent flows, respectively. The conclusions, nevertheless, are applicable when using the parabolized stability equations (PSEs) (e.g., [5]), although the PSEs are appropriate only for the treatment of convective instability and not absolute instability [34]. They are also applicable to both base and mean flows although there are important differences between the results for these profiles which will be drawn out. The temporal mean velocity profiles are known throughout the domain from numerical simulation for the cylinder flow while they are obtained via an eddy viscosity model (e.g., [35]) for the turbulent channel flow. We begin by considering the general case in which there exists invariance only in time. In other words, the analysis is performed in the frequency domain, such that mode shapes may be functions of all three spatial dimensions. Decomposition into spatial wavenumbers is applied in the case of wall-bounded turbulent flows with streamwise and spanwise periodicity in Sec. V.

A. Eigenmode decomposition

The classical (temporal) linear stability analysis, detailed, for example, in [13], proceeds under the assumption of small perturbations to the steady state. It has been performed relative to both base and mean flows in order to determine frequencies subject to exponential growth (instability). See, e.g., [36] for further details. Substituting perturbations of the form

$$\boldsymbol{u}(\boldsymbol{x},t) = \overline{\boldsymbol{u}}(\boldsymbol{x}) + \epsilon \tilde{\boldsymbol{u}}(\boldsymbol{x}) \exp(\lambda t), \tag{4}$$

where $\epsilon \ll 1$, into Eq. (1) yields, at $O(\epsilon)$,

$$\lambda \tilde{\boldsymbol{u}} = -\overline{\boldsymbol{u}} \cdot \nabla \tilde{\boldsymbol{u}} - \tilde{\boldsymbol{u}} \cdot \nabla \overline{\boldsymbol{u}} - \nabla \tilde{p} + \mathrm{Re}^{-1} \nabla^2 \tilde{\boldsymbol{u}}, \tag{5a}$$

$$\nabla \cdot \tilde{\boldsymbol{u}} = 0, \tag{5b}$$

TABLE I. Operator form of the equations for stability and resolvent analyses. Variables with a tilde correspond to stability analysis while a caret indicates resolvent analysis.

	Base flow	Mean flow
Stability analysis	$\lambda \boldsymbol{B}\begin{pmatrix}\tilde{\boldsymbol{u}}\\ \tilde{p}\end{pmatrix} = \boldsymbol{A}\begin{pmatrix}\tilde{\boldsymbol{u}}\\ \tilde{p}\end{pmatrix}$	$\lambda \boldsymbol{B}\begin{pmatrix}\tilde{\boldsymbol{u}}\\ \tilde{p}\end{pmatrix} = \boldsymbol{L}\begin{pmatrix}\tilde{\boldsymbol{u}}\\ \tilde{p}\end{pmatrix}$
Resolvent analysis	$i\omega \boldsymbol{B}\begin{pmatrix}\hat{\boldsymbol{u}}\\ \hat{p}\end{pmatrix} = \boldsymbol{A}\begin{pmatrix}\hat{\boldsymbol{u}}\\ \hat{p}\end{pmatrix} + \boldsymbol{C}\hat{\boldsymbol{f}}$	$i\omega \boldsymbol{B}\begin{pmatrix}\hat{\boldsymbol{u}}\\ \hat{p}\end{pmatrix} = \boldsymbol{L}\begin{pmatrix}\hat{\boldsymbol{u}}\\ \hat{p}\end{pmatrix} + \boldsymbol{C}\hat{\boldsymbol{f}}$

where a tilde is used to denote that a stability analysis has been performed. Written explicitly for base flows in operator form, one obtains

$$\lambda \boldsymbol{B}\begin{pmatrix}\tilde{\boldsymbol{u}}\\ \tilde{p}\end{pmatrix} = \boldsymbol{A}\begin{pmatrix}\tilde{\boldsymbol{u}}\\ \tilde{p}\end{pmatrix}, \tag{6}$$

where $\boldsymbol{A}$ is the LNS operator with respect to the base flow,

$$\boldsymbol{A} = \begin{pmatrix}-\boldsymbol{U}_0 \cdot \nabla() - () \cdot \nabla \boldsymbol{U}_0 + \mathrm{Re}^{-1}\nabla^2() & -\nabla() \\ \nabla \cdot () & 0\end{pmatrix}, \tag{7}$$

and

$$\boldsymbol{B} = \begin{pmatrix}1 & 0\\ 0 & 0\end{pmatrix}. \tag{8}$$

Similarly, we use $\boldsymbol{L}$ to denote the LNS operator with respect to the mean flow, such that for mean flow stability analysis

$$\lambda \boldsymbol{B}\begin{pmatrix}\tilde{\boldsymbol{u}}\\ \tilde{p}\end{pmatrix} = \boldsymbol{L}\begin{pmatrix}\tilde{\boldsymbol{u}}\\ \tilde{p}\end{pmatrix}, \tag{9}$$

with

$$\boldsymbol{L} = \begin{pmatrix}-\overline{\boldsymbol{u}} \cdot \nabla() - () \cdot \nabla \overline{\boldsymbol{u}} + \mathrm{Re}^{-1}\nabla^2() & -\nabla() \\ \nabla \cdot () & 0\end{pmatrix}. \tag{10}$$

The resulting eigenvalue problems for base and mean flows are summarized in the top row of Table I. Stability analysis is based on the spectrum of the LNS operator and λ is an indicator of the linear stability of a given profile. The eigenvectors may be used as a basis for modal decomposition.

The adjoint NSEs have been derived by, e.g., [37], and the linearized operators can be written for both base and mean flows, $\boldsymbol{A}^*$ and $\boldsymbol{L}^*$, respectively, for the adjoint variables $\tilde{\boldsymbol{v}}$ and $\tilde{q}$:

$$\boldsymbol{A}^* = \begin{pmatrix}\boldsymbol{U}_0 \cdot \nabla() - () \cdot (\nabla \boldsymbol{U}_0)^* + \mathrm{Re}^{-1}\nabla^2() & \nabla() \\ \nabla \cdot () & 0\end{pmatrix}, \tag{11}$$

$$\boldsymbol{L}^* = \begin{pmatrix}\overline{\boldsymbol{u}} \cdot \nabla() - () \cdot (\nabla \overline{\boldsymbol{u}})^* + \mathrm{Re}^{-1}\nabla^2() & \nabla() \\ \nabla \cdot () & 0\end{pmatrix}. \tag{12}$$

The operators satisfy

$$\langle \tilde{\boldsymbol{u}}, \boldsymbol{A}\tilde{\boldsymbol{v}} \rangle = \langle \boldsymbol{A}^*\tilde{\boldsymbol{u}}, \tilde{\boldsymbol{v}} \rangle, \tag{13}$$

$$\langle \tilde{\boldsymbol{u}}, \boldsymbol{L}\tilde{\boldsymbol{v}} \rangle = \langle \boldsymbol{L}^*\tilde{\boldsymbol{u}}, \tilde{\boldsymbol{v}} \rangle, \tag{14}$$

where $\langle\,,\rangle$ is the scalar product associated with the energy in the whole domain.

For a general operator, $\boldsymbol{T}$, that is normal, i.e., $\boldsymbol{T}\boldsymbol{T}^* = \boldsymbol{T}^*\boldsymbol{T}$, the eigenvectors of $\boldsymbol{T}$ corresponding to distinct eigenvalues are orthogonal although the eigenvalues may be complex. Self-adjoint operators ($\boldsymbol{T} = \boldsymbol{T}^*$), on the other hand, have orthogonal eigenvectors and real eigenvalues. In general, the LNS

operators $\boldsymbol{A}$ and $\boldsymbol{L}$ are neither self-adjoint nor normal. These phenomena account for the differences between Eqs. (7) and (10) and Eqs. (11) and (12).

B. Resolvent analysis

For the more general case when the perturbation cannot be considered to be infinitesimal and the nonlinearity $\boldsymbol{f}'$ is retained, Eq. (3a) can be rewritten in terms of a transfer function between the forcing (input) and response state (output) (e.g., [13,14,17]). This transfer function is the (linear) resolvent operator, which can be defined around either the base or mean flow (see Table I).

For harmonic forcing and response at temporal frequency ω,

$$\boldsymbol{f}' = \hat{\boldsymbol{f}} \exp(i\omega t), \quad \boldsymbol{u}' = \hat{\boldsymbol{u}} \exp(i\omega t), \tag{15}$$

and a base flow profile, $\overline{\boldsymbol{u}} = \boldsymbol{U}_0$,

$$\hat{\boldsymbol{u}} = \mathcal{H}(\omega)\hat{\boldsymbol{f}}, \tag{16}$$

where the caret denotes that the perturbation is associated with a resolvent analysis. The resolvent operator is given by

$$\mathcal{H}(\omega) = \boldsymbol{C}^T(i\omega\boldsymbol{B} - \boldsymbol{A})^{-1}\boldsymbol{C}, \tag{17}$$

where

$$\boldsymbol{C} = \begin{pmatrix} 1 \\ 0 \end{pmatrix}. \tag{18}$$

Similarly, for a mean flow,

$$\mathcal{H}(\omega) = \boldsymbol{C}^T(i\omega\boldsymbol{B} - \boldsymbol{L})^{-1}\boldsymbol{C}. \tag{19}$$

It should be noted that the sense of the imaginary and real parts of ω is reversed in the resolvent analysis relative to the definition customary to the stability literature of Eq. (4): here the real part of ω is the frequency associated with a mode while the imaginary part is set to zero as only neutral disturbances are considered. In stability analysis, the imaginary part of λ is the frequency of the disturbance and the real part is the growth rate.

$\mathcal{H}(\omega)$ can be decomposed via a singular value decomposition (SVD) (e.g., [17]),

$$\mathcal{H}(\omega) = \boldsymbol{\Psi}(\omega)\boldsymbol{\Sigma}(\omega)\boldsymbol{\Phi}^*(\omega), \tag{20}$$

where $\boldsymbol{\Psi}$ and $\boldsymbol{\Phi}$ are the left and right singular vectors corresponding to the response and forcing modes, often called resolvent modes (see [17]), respectively. Both sets of singular vectors are guaranteed to be orthonormal bases and are ranked according to their gain, or singular value, contained in the diagonal matrix $\boldsymbol{\Sigma}$. The resolvent operator can thus be written as the sum of outer products of the left and right singular vectors:

$$\mathcal{H}(\omega) = \sum_{j=1}^{\infty} \hat{\boldsymbol{\psi}}_j(\omega)\sigma_j(\omega)\hat{\boldsymbol{\phi}}_j^*(\omega). \tag{21}$$

$\mathcal{H}(\omega)$ is (approximately) low rank if

$$\sum_{j=1}^{p} \sigma_j^2 \approx \sum_{j=1}^{\infty} \sigma_j^2, \tag{22}$$

where $\sigma_p \gg \sigma_{p+1}$ and p is small [33,38]. If the leading singular value, or resolvent norm, is significantly greater than all others ($\sigma_1 \gg \sigma_2$) then the rank-1 approximation can be invoked and the resolvent is approximated by the outer product of the leading optimal response and forcing modes:

$$\mathcal{H}(\omega) \approx \sigma_1 \hat{\boldsymbol{\psi}}_1 \hat{\boldsymbol{\phi}}_1^*. \tag{23}$$

The physical interpretation of the resolvent response modes is the response to forcing that results in a neutrally stable response, i.e., with the real component of frequency equal to zero. The singular value gives the input-output gain, here associated with the energy norm.

C. Amplification mechanisms

The origin of the amplification mechanisms can be identified by expanding the resolvent through an eigenvalue decomposition of the LNS operator,

$$\mathcal{H}(\omega) = \boldsymbol{C}^T(i\omega\boldsymbol{B} - \boldsymbol{V}\boldsymbol{\Lambda}\boldsymbol{B}\boldsymbol{V}^{-1})^{-1}\boldsymbol{C}. \tag{24}$$

Here $\boldsymbol{V}$ represents the matrix of eigenvectors of the LNS operator for either the base or mean flow profile and $\boldsymbol{\Lambda}$ the diagonal matrix of eigenvalues. These can be used to find an upper and lower bound for the resolvent norm (see [13]):

$$\|i\omega\boldsymbol{I} - \boldsymbol{\Lambda}\|^{-1} \leqslant \|\mathcal{H}(\omega)\| \leqslant \underbrace{\|\boldsymbol{V}\|\|\boldsymbol{V}^{-1}\|}_{\text{pseudoresonance}}\underbrace{\|i\omega\boldsymbol{I} - \boldsymbol{\Lambda}\|^{-1}}_{\text{resonance}}, \tag{25}$$

where $\|\cdot\|$ is the (operator) 2-norm. The far-right-hand term in Eq. (25) is forcing in the vicinity of an eigenvalue, i.e., $\omega = \lambda$, or amplification due to resonance, which is predictable from an eigenanalysis. Large amplification also arises in the event of pseudoresonance when the condition number $\kappa = \|\boldsymbol{V}\|\|\boldsymbol{V}^{-1}\|$ is large due to nonorthogonality of the eigenvectors, a consequence of the non-normal nature of $\boldsymbol{L}$ and hence $\mathcal{H}(\omega)$. In the formulation of Eq. (25), the resolvent therefore contains both the amplification mechanisms associated with the eigenvalue spectrum accessed via eigenanalysis (normal mode linear stability analysis) and the pseudoresonant amplification that is possible when the eigenvectors are not orthogonal to each other.

To begin a review of known amplification mechanisms, we first consider flows without streamwise development where $\boldsymbol{U}_0 = U_0(y)$ or $\overline{\boldsymbol{u}} = \overline{u}(y)$. When an amplification mechanism is purely normal, the forcing and response modes are identical as seen in Figs. 1(a) and 1(b). Brandt *et al.* [39] described a component-type non-normality (this term originated with Marquet *et al.* [40] in the context of forward and adjoint eigenmodes), which distributes energy in different velocity components of the forcing and response modes. The root of this non-normality is the mean shear term $\partial\overline{u}/\partial y$ in the LNS operator. Figures 1(c) and 1(d) show a cartoon of the lift-up mechanism [41], where a disturbance concentrated in v leads to a response in u. In the absence of shear, the LNS operator is still not self-adjoint due to the mean flow advection term resulting in a phase difference between the forcing and response modes as seen in Figs. 1(e) and 1(f). When both mean shear and mean flow advection are nonzero, one observes the Orr mechanism [42], which reorients upstream-leaning forcing modes with the mean shear such that the response modes are leaning downstream [43] as seen in Figs. 1(g) and 1(h).

For a flow with streamwise development, Chomaz [26] identified a convective-type non-normality separating the spatial support of forcing and response modes, with the latter being downstream of the former. The source of this non-normality is mean flow advection since the adjoint of the derivative operator introduces a negative sign, implying that adjoint perturbations are transported upstream. Forward perturbations are transported downstream. For absolutely unstable flows, for which perturbations grow both upstream and downstream of the source, the advection term may no longer separate the spatial support of the adjoint and forward modes, leading to regions of overlap at resonant frequencies. This region, known as the wavemaker for base flows, is associated with nonzero values of $\mathcal{W}$, where

$$\mathcal{W}(\boldsymbol{x}_0) = \|\tilde{\boldsymbol{u}}(\boldsymbol{x}_0)\|\|\tilde{\boldsymbol{v}}(\boldsymbol{x}_0)\|, \tag{26}$$

and $\boldsymbol{x}_0$ denotes a position in space (see derivation of [31]). Meliga *et al.* [44] identified a wavemaker in the context of the mean cylinder wake, interpreting it as a sensitivity map of the vortex shedding frequency and amplitude. In the context of resolvent analysis, Brandt *et al.* [39] noted that the overlap of forcing and response modes is a qualitative proxy for sensitivity of the resolvent norm to base

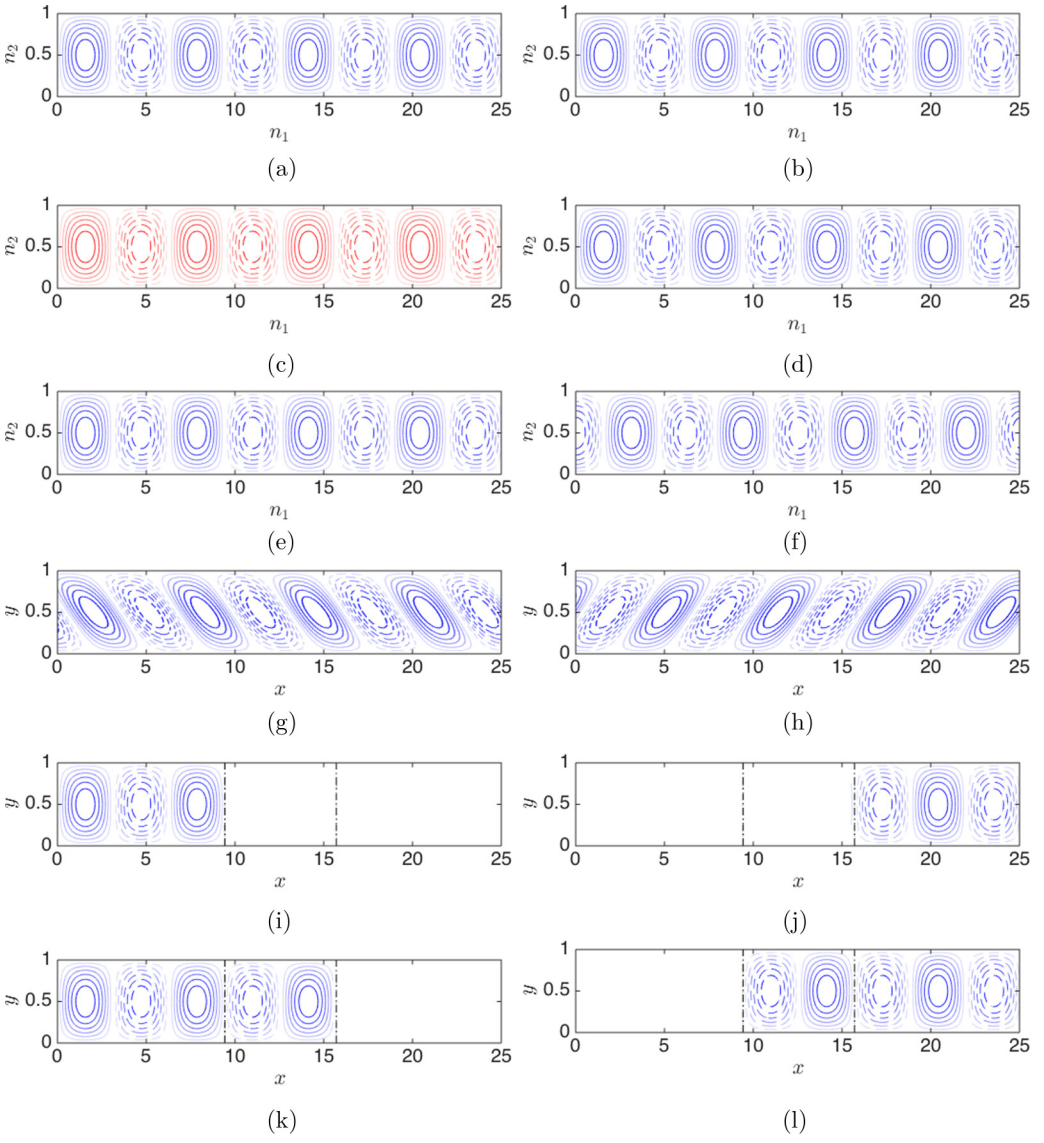

FIG. 1. Cartoon of forcing (left) and response (right) modes corresponding to various amplification mechanisms. (a), (b) Purely normal mechanism where the modes are identical; (c), (d) component-type non-normality due to the lift-up mechanism. (e), (f) A $\pi/2$ phase shift between the modes due to the non-self-adjoint nature of the LNS operator. When coupled with mean shear, this results in the (g), (h) Orr mechanism, where the forcing mode leans upstream against the mean shear and the response mode leans downstream with the mean shear. (i), (j) A convective-type non-normality where mean flow advection results in the forcing being upstream of the response. (k), (l) The vertical dash-dotted lines denote the region where the forcing and response modes overlap in the streamwise direction. The flow is said to be absolutely unstable in this region and convectively unstable elsewhere. Positive (negative) isocontours are denoted by solid (dotted) lines and blue (red) indicates streamwise (transverse) components, in the x, y directions, respectively. Each mode is nonzero in one velocity component only.

flow modifications. Qadri and Schmid [27] derived an expression for the sensitivity of σ_1 to small localized changes in the governing equations

$$\nabla_{\boldsymbol{A}}\sigma_1 = \sigma_1^2 \mathrm{Real}(\hat{\phi}_{1,i}\hat{\psi}^*_{1,j}), \tag{27}$$

where the subscripts i and j are the velocity component of the forcing or response, respectively. In the event that the resolvent identifies eigenmodes as the most amplified forcing and response, the wavemaker computed by $\|\hat{\boldsymbol{\psi}}_1(\boldsymbol{x}_0)\|\|\hat{\boldsymbol{\phi}}_1(\boldsymbol{x}_0)\|$ can be interpreted as the degree to which the resolvent norm is sensitive at a spatial location to modifications of the LNS operator.

The wavemaker approximates regions of the flow which are absolutely unstable or self-sustaining since perturbations are prevented from convecting due to reverse flow [45]. If the flow is convectively unstable, there is no region of reverse flow and so $\overline{\boldsymbol{u}}$ is always positive. In this case, the optimal response or stability mode will be downstream of the optimal forcing or adjoint mode as depicted in Figs. 1(i) and 1(j). Huerre and Monkewitz [29] have shown that when a mean profile of hyperbolic tangent form exhibits greater than 13.6% reverse flow with respect to the free stream, the flow is absolutely unstable. The streamwise extent of absolute instability and the wavemaker is finite since flow reversal is confined to a certain portion of the flow as illustrated by the cartoon in Figs. 1(k) and 1(l). This information is encoded within the advection term $\overline{\boldsymbol{u}}\cdot\nabla()$ through the sign of $\overline{\boldsymbol{u}}$.

D. Spectrum and pseudospectrum of the LNS operator

Analyzing the resolvent corresponds to considering the spectrum of the perturbed LNS operator:

$$\Lambda_\epsilon(\boldsymbol{A}) = \{z \in \mathbb{C} : z \in \Lambda(\boldsymbol{A}+\boldsymbol{E}) \text{ where} \|\boldsymbol{E}\| \leqslant \epsilon\}, \tag{28}$$

where Λ_ϵ is the pseudospectrum of $\boldsymbol{A}$ under a perturbation magnitude $\epsilon > 0$ [12,22,36]. An equivalent definition is given by

$$\Lambda_\epsilon(\boldsymbol{A}) = \{z \in \mathbb{C} : \|(z\boldsymbol{I}-\boldsymbol{A})^{-1}\| \geqslant \epsilon^{-1}\} \cup \Lambda(\boldsymbol{A}), \tag{29}$$

where $\Lambda = \Lambda_0$ is the spectrum of $\boldsymbol{A}$. Throughout the paper, we use Λ to represent the set of eigenvalues and $\boldsymbol{\Lambda}$ the diagonal matrix of eigenvalues. If $\boldsymbol{A}$ is normal, Λ_ϵ can be interpreted as the set of points away from Λ by only less than or equal to ϵ on the complex plane (see [36]). If $\boldsymbol{A}$ is non-normal, this distance may be greater than ϵ, signifying that an eigenvalue is sensitive to perturbation of the LNS operator.

III. RESOLVENT NORM AND THE SPECTRUM

In this section, the conditions under which analysis of the resolvent is likely to identify stability modes as the most amplified disturbance are formalized and scalar measures of non-normality are introduced. We also highlight when the rank-1 approximation is appropriate for amplifications which are resonant in character. Two-by-two example operators highlight trends with respect to how resolvent modes project onto eigenmodes and how the spectrum is related to the resolvent norm.

A. Dyad expansion of the resolvent operator

As is more customary for the eigenvalue problem [25,37], a dyad expansion of the resolvent $\boldsymbol{R}$ for a generic, nonsingular linear operator $\boldsymbol{Q}$ can be performed:

$$\boldsymbol{R} = (z\boldsymbol{I}-\boldsymbol{Q})^{-1} = \sum_{j=1}^{n} \frac{1}{z-\lambda_j}\tilde{\boldsymbol{g}}_j\tilde{\boldsymbol{h}}_j^*, \tag{30}$$

where $\tilde{\boldsymbol{g}}_j$ and $\tilde{\boldsymbol{h}}_j$ are the jth left and right eigenvectors of $\boldsymbol{Q}$, respectively. Since the objective of resolvent analysis is often the identification of the most amplified neutral disturbance, $i\omega$ is substituted

for z and the eigenvectors of the LNS operator for $\tilde{\boldsymbol{g}}_j$ and $\tilde{\boldsymbol{h}}_j$ into Eq. (30) to give

$$\mathcal{H}(\omega) = \sum_{j=1}^{n} \frac{1}{i\omega - \lambda_j} \tilde{\boldsymbol{u}}_j \tilde{\boldsymbol{v}}_j^*. \tag{31}$$

Thus if the real part of an eigenvalue λ_p is sufficiently close to zero and the forcing frequency ω is identical to the imaginary part, then its contribution to the series dominates over the contributions from all other eigenvalues. The resolvent, furthermore, can be approximated by the forward and adjoint eigenvectors corresponding to that frequency weighted by the inverse distance between the eigenvalue and the imaginary axis:

$$\mathcal{H}(\omega) \approx \frac{1}{i\omega - \lambda_p} \tilde{\boldsymbol{u}}_p \tilde{\boldsymbol{v}}_p^*. \tag{32}$$

Equation (32) represents a rank-1 approximation of the resolvent operator using eigenvectors. In the context of base flows, the resolvent is singular at the critical Reynolds number since the real part of the least stable eigenvalue is identically zero when it crosses the imaginary axis. In the case of mean flows, which tend to be marginally stable (e.g., [1,6,35]), Eq. (32) is applicable for eigenvalues near the imaginary axis. It is important to note that an eigenvalue does not have to be marginally stable, but it must be the dominant contribution to the series in Eq. (31). It is possible to obtain a rank-1 approximation of the resolvent even when an eigenvalue is highly damped, as seen in Sec. IV.

This rank-1 approximation fails when there is not sufficient separation of eigenvalues at the frequency of interest. If there are several eigenvalues in the vicinity of the imaginary axis at a frequency ω, then the resolvent operator can no longer be approximated by just one outer product in Eq. (32). Equating the two low-rank approximations of the resolvent operator in terms of eigenvectors [Eq. (32)] and resolvent modes [Eq. (23)] implies the following:

$$\sigma_1 \hat{\boldsymbol{\psi}}_1 \hat{\boldsymbol{\phi}}_1^* \approx \frac{1}{i\omega - \lambda_r} \tilde{\boldsymbol{u}}_r \tilde{\boldsymbol{v}}_r^* \Rightarrow \hat{\boldsymbol{\psi}}_1 \propto \tilde{\boldsymbol{u}}_r, \ \hat{\boldsymbol{\phi}}_1 \propto \tilde{\boldsymbol{v}}_r, \tag{33}$$

since

$$\hat{\boldsymbol{\psi}}_1 \approx \frac{1}{\sigma_1 (i\omega - \lambda_r)} \tilde{\boldsymbol{u}}_r \tilde{\boldsymbol{v}}_r^* \hat{\boldsymbol{\phi}}_1 = \beta \tilde{\boldsymbol{u}}_r, \tag{34}$$

where β is a complex constant. The leading resolvent response and forcing modes are proportional to the forward and adjoint eigenmodes, respectively, and this holds for any base or mean flow as long as only one eigenvalue leads to amplification. The similarity between the resolvent forcing and adjoint stability modes draws out how the resolvent operator contains sensitivity information, as described by, e.g., [27]. The development is less amenable for pseudoresonant mechanisms where the proximity of an eigenvalue to the imaginary axis does not necessarily govern the behavior of the resolvent. It is argued in Sec. III E that pseudoresonant mechanisms generally correspond to a low-rank operator.

B. The relationship between spectral radius and spectral norm for approximately low-rank operators

For a nonsingular linear operator $\boldsymbol{Q}$, we now seek to find an explicit relationship between the spectrum of $\boldsymbol{Q}$ and the spectral norm of its resolvent $\boldsymbol{R}(z) = (z\boldsymbol{I} - \boldsymbol{Q})^{-1}$. We are particularly interested in cases where $\boldsymbol{R}(z)$ is approximately low rank (i.e., a small number of leading singular values are much larger than the others).

The spectral radius ρ of an operator $\boldsymbol{Q}$ can be defined through the eigendecomposition $\boldsymbol{V}\boldsymbol{\Lambda}\boldsymbol{V}^{-1}$:

$$\rho(\boldsymbol{Q}) = \max_{\lambda_j \in \boldsymbol{\Lambda}}(|\lambda_j|). \tag{35}$$

The spectral radius of the corresponding resolvent operator is

$$\rho(\boldsymbol{R}(z)) = \max_{\lambda_j \in \boldsymbol{\Lambda}}(|z-\lambda_j|^{-1}) = \left[\min_{\lambda_j \in \boldsymbol{\Lambda}}(|z-\lambda_j|)\right]^{-1}. \tag{36}$$

Note that, with this definition, Eq. (25) may be expressed as

$$\rho(\boldsymbol{R}) \leqslant \sigma_1 \leqslant \kappa\rho(\boldsymbol{R}).$$

For non-normal operators with large condition numbers, the upper and lower bounds span a large range and thus do not give much insight into the size of the resolvent norm, σ_1. To estimate the resolvent norm in terms of the spectral radius, we make use of the relationship [46]

$$\rho(\boldsymbol{R}) = \lim_{n\to\infty} \|\boldsymbol{R}^n\|^{1/n}. \tag{37}$$

Suppose now that the largest singular value of resolvent operator (for a given z) is much larger than the rest, such that

$$\boldsymbol{R}(z) = \boldsymbol{\Psi}\boldsymbol{\Sigma}\boldsymbol{\Phi}^* \approx \boldsymbol{\Psi}\boldsymbol{\Sigma}_1\boldsymbol{\Phi}^*,$$

where $\boldsymbol{\Sigma}_1$ is $\boldsymbol{\Sigma}$ with all but the first singular value set to zero.

Suppose in addition that this truncation is also accurate for powers of $\boldsymbol{R}$, i.e., that we have

$$\boldsymbol{R}^n \approx (\boldsymbol{\Psi}\boldsymbol{\Sigma}_1\boldsymbol{\Phi}^*)^n. \tag{38}$$

Defining the quantity

$$r_{ij} = \frac{\hat{\boldsymbol{\phi}}_i^*\hat{\boldsymbol{\psi}}_j}{\hat{\boldsymbol{\phi}}_j^*\hat{\boldsymbol{\psi}}_j},$$

we then have

$$(\boldsymbol{\Phi}^*\boldsymbol{\Psi}\boldsymbol{\Sigma}_1)^n = \sigma_1^n(\hat{\boldsymbol{\phi}}_1^*\hat{\boldsymbol{\psi}}_1)^n \begin{pmatrix} r_{11} & 0 & \cdots & 0 \\ r_{21} & 0 & \cdots & 0 \\ \vdots & \vdots & \ddots & \vdots \end{pmatrix}.$$

We may now estimate the norm of powers of the resolvent as

$$\begin{aligned} \|\boldsymbol{R}^n\| &= \|\boldsymbol{\Phi}^*\boldsymbol{R}^n\boldsymbol{\Phi}\| \\ &\approx \|(\boldsymbol{\Phi}^*\boldsymbol{\Psi}\boldsymbol{\Sigma}_1)^n\| \\ &= \sigma_1^n|\hat{\boldsymbol{\phi}}_1^*\hat{\boldsymbol{\psi}}_1|^{n-1}\|\boldsymbol{r}\|, \end{aligned}$$

where $\boldsymbol{r} = [r_{11}\ r_{21}\ \cdots]^T$, and we have used the fact that $\boldsymbol{\Phi}$ is unitary. Consequently, assuming that Eq. (38) holds, Eq. (37) results in the estimate

$$\rho(\boldsymbol{R}) \approx \sigma_1|\hat{\boldsymbol{\phi}}_1^*\hat{\boldsymbol{\psi}}_1|. \tag{39}$$

In other words, we may estimate that the resolvent norm is larger than the lower bound in Eq. (25) by a factor of $|\hat{\boldsymbol{\phi}}_1^*\hat{\boldsymbol{\psi}}_1|^{-1}$. This analysis relied on the rather restrictive assumption that only the leading singular value was large. If there is a pair of large singular values, as is often the case in channel flows (owing to spatial symmetry across the mid-plane of the channel), then we may generalize the argument as follows. Suppose that σ_1 and σ_2 are of comparable size, and that all other singular values

are negligibly small. If we further assume that $|\hat{\boldsymbol{\phi}}_1^* \hat{\boldsymbol{\psi}}_2|$, $|\hat{\boldsymbol{\phi}}_2^* \hat{\boldsymbol{\psi}}_1| \approx 0$, then we find that

$$(\boldsymbol{\Phi}^* \boldsymbol{\Psi} \boldsymbol{\Sigma})^n \approx \begin{pmatrix} \sigma_1 \hat{\boldsymbol{\phi}}_1^* \hat{\boldsymbol{\psi}}_1 & \sigma_2 \hat{\boldsymbol{\phi}}_1^* \hat{\boldsymbol{\psi}}_2 & 0 & \cdots & 0 \\ \sigma_1 \hat{\boldsymbol{\phi}}_2^* \hat{\boldsymbol{\psi}}_1 & \sigma_2 \hat{\boldsymbol{\phi}}_2^* \hat{\boldsymbol{\psi}}_2 & 0 & \cdots & 0 \\ \vdots & \vdots & \vdots & \ddots & \vdots \end{pmatrix}^n$$

$$\approx \sigma_1^n |\hat{\boldsymbol{\phi}}_1^* \hat{\boldsymbol{\psi}}_1|^{n-1} \begin{pmatrix} r_{11} & 0 & \cdots & 0 \\ r_{21} & 0 & \cdots & 0 \\ \vdots & \vdots & \ddots & \vdots \end{pmatrix} + \sigma_2^n |\hat{\boldsymbol{\phi}}_2^* \hat{\boldsymbol{\psi}}_2|^{n-1} \begin{pmatrix} 0 & r_{12} & 0 & \cdots & 0 \\ 0 & r_{22} & 0 & \cdots & 0 \\ \vdots & \vdots & \vdots & \ddots & \vdots \end{pmatrix},$$

which, following the same approach as before, gives

$$\rho(\boldsymbol{R}) \approx \max\{\sigma_1 |\hat{\boldsymbol{\phi}}_1^* \hat{\boldsymbol{\psi}}_1|, \sigma_2 |\hat{\boldsymbol{\phi}}_2^* \hat{\boldsymbol{\psi}}_2|\}. \tag{40}$$

Thus the inverse of $|\hat{\boldsymbol{\phi}}_1^* \hat{\boldsymbol{\psi}}_1|$ can be interpreted as the contribution of non-normality to the resolvent norm. We can also identify the product $\sigma_1 |i\omega - \lambda|$ as a quantification of non-normality since $|i\omega - \lambda|^{-1}$ represents the resonance contribution to the resolvent norm. However, since highly amplified modes may occur at nonresonant frequencies, the contribution from $|i\omega - \lambda|$ is typically overestimated as it is likely for a pseudoeigenvalue to reside much closer to the imaginary axis than the nearest eigenvalue of the unperturbed spectrum. Other scalar measures of non-normality have been proposed, e.g., by Trefethen and Embree [47], but are not investigated here. As shown in Secs. IV and V, these two predictions tend to agree in cases where amplification can be attributed to a single eigenvalue and mean stability analysis is valid.

C. Asymptotic limits of the influence of the lift-up mechanism

We specialize now to operators with similar behavior to the LNS system and consider the associated features of eigenvector and singular value decompositions. We choose a model operator with characteristics similar to the LNS, in the vein of that explored by Gebhardt and Grossmann [48]. The LNS for the two-dimensional velocity field associated with a one-dimensional base or mean flow variation takes a similar form to $\boldsymbol{M}$, where

$$\boldsymbol{M} = \begin{pmatrix} m_1 & d \\ 0 & m_2 \end{pmatrix}. \tag{41}$$

By selecting a one-dimensional operator, we have elected to neglect spatial (streamwise and spanwise) dependence of the base flow and therefore the modes themselves here. Nevertheless, the impact of the various types of term in the LNS operator on the resolvent modes can be modeled. Here $\mathrm{Real}(m_j) < 0$ is analogous to the stabilizing role of viscosity through the $\mathrm{Re}^{-1}\nabla^2(\,)$ term and $\mathrm{Imag}(m_j)$ represents mean flow advection through the $-\overline{\boldsymbol{u}} \cdot \nabla(\,)$ term. d is real and is analogous to mean shear $(\,) \cdot \nabla \overline{\boldsymbol{u}}$, which here is equal to the gradient in the 2-direction of mean flow in the 1-direction. Thus in this simple two-by-two example, d models the lift-up mechanism [41] by coupling forcing in the n_2 direction (second component of the vector) with a response in the n_1 direction (first component of the vector).

The resolvent of $\boldsymbol{M}$ is

$$\mathcal{H}(\omega) = \begin{pmatrix} -1/(m_1 - i\omega) & d/[(m_1 - i\omega)(m_2 - i\omega)] \\ 0 & -1/(m_2 - i\omega) \end{pmatrix}. \tag{42}$$

In order to isolate the effect of lift-up introduced via the off-diagonal term in Eq. (43), the eigenvalues are assumed to be real and we limit the immediate development to stationary disturbances ($\omega = 0$)

to eliminate the remaining imaginary terms, such that

$$\mathcal{H}(\omega = 0) = \begin{pmatrix} -1/(m_1) & d/[(m_1 m_2)] \\ 0 & -1/(m_2) \end{pmatrix}. \tag{43}$$

For the limiting case of $d = 0$, i.e., no lift-up, $\boldsymbol{M}$ and its resolvent are self-adjoint and therefore normal. If the least stable eigenvalue has a real part close to zero which would occur, say, if $m_1 \to 0$, the singular value decomposition can be simplified to

$$\lim_{m_1 \to 0} \mathrm{SVD}(\mathcal{H}(\omega = 0)) = \begin{pmatrix} 1 & 0 \\ 0 & 1 \end{pmatrix} \begin{pmatrix} \sigma_1 & 0 \\ 0 & \sigma_2 \end{pmatrix} \begin{pmatrix} 1 & 0 \\ 0 & 1 \end{pmatrix}, \tag{44}$$

where $\sigma_1/\sigma_2 \to \infty$; i.e., the resolvent is low rank and the response can be well predicted from the leading singular vectors $\hat{\boldsymbol{\psi}}_1$ and $\hat{\boldsymbol{\phi}}_1$. For a normal operator, these are identical to each other, $\hat{\boldsymbol{\psi}}_1 = \hat{\boldsymbol{\phi}}_1 = [1 \;\; 0]^T$, and identical to the corresponding eigenvectors as seen in Figs. 1(a) and 1(b). The inner product $|\hat{\boldsymbol{\phi}}_1^* \hat{\boldsymbol{\psi}}_1|$ quantifies the componentwise correspondence between the forcing and response modes which, in this limit, is equal to unity. In the limit $d \to \infty$

$$\lim_{d \to \infty} \mathrm{SVD}(\mathcal{H}(\omega = 0)) = \begin{pmatrix} 1-\gamma & -\delta \\ \delta & 1-\gamma \end{pmatrix} \begin{pmatrix} \sigma_1 & 0 \\ 0 & \sigma_2 \end{pmatrix} \begin{pmatrix} \delta & \gamma - 1 \\ 1-\gamma & \delta \end{pmatrix}, \tag{45}$$

where $\sigma_1/\sigma_2 \to \infty$ and $\delta, \gamma \to 0$. The constants δ and γ are real and positive. The resolvent operator is still low rank in this limit, but $\hat{\boldsymbol{\psi}}_1$ and $\hat{\boldsymbol{\phi}}_1$ are now orthogonal to each other and thus $|\hat{\boldsymbol{\phi}}_1^* \hat{\boldsymbol{\psi}}_1| \to 0$. The perturbation energy in the optimal forcing mode is concentrated in the second component of the vector while the perturbation energy in the optimal response mode is concentrated in the first component, as sketched in Figs. 1(c) and 1(d).

The analogous eigenvalue decomposition of (non-normal) $\boldsymbol{M}$ is

$$\lim_{d \to \infty} \mathrm{EIG}(\boldsymbol{M}) = \begin{pmatrix} 1 & 1 \\ 0 & \alpha \end{pmatrix} \begin{pmatrix} m_1 & 0 \\ 0 & m_2 \end{pmatrix} \begin{pmatrix} 1 & -1/\alpha \\ 0 & 1/\alpha \end{pmatrix}, \tag{46}$$

where $\alpha \to 0$ is a positive, real constant. Unlike the resolvent response modes which are orthogonal to one another, the eigenvectors are nonorthogonal, such that $\kappa \to \infty$. In this case, the stability and resolvent modes are different and it is not clear from the eigenmode decomposition that the resolvent operator is low rank. Since the eigenvectors are nearly parallel, they both project equally well onto the optimal resolvent response mode. The same can be said for the projection of the adjoint modes, which are also nearly parallel, onto the optimal resolvent forcing mode. As seen for the example operators below, it is desirable for the most amplified resolvent mode to project onto as many eigenmodes as possible, just as they do for this limiting case, to maximize the resolvent norm. It is much more efficient, consequently, to use resolvent modes as a basis for low-order models as opposed to eigenmodes.

D. Resonance curve and resolvent norm

To demonstrate the amplification characteristics of the resolvent for normal and non-normal operators, we sketch in Fig. 2 the pseudospectra for simple example operators,

$$\boldsymbol{S} = \begin{pmatrix} -1.5 + 1.1i & 0 \\ 0 & -1.9 - 2.2i \end{pmatrix}, \tag{47}$$

$$\boldsymbol{P} = \begin{pmatrix} -1.5 + 1.1i & 5 \\ 0 & -1.9 - 2.2i \end{pmatrix}, \tag{48}$$

where $\boldsymbol{S}$ is a normal operator containing only the eigenvalues of the non-normal operator $\boldsymbol{P}$. Level curves of ϵ for operators $\boldsymbol{S}$ and $\boldsymbol{P}$ satisfy

$$\Lambda_\epsilon(\boldsymbol{S}) = \{z \in \mathbb{C} : \|(z\boldsymbol{I} - \boldsymbol{S})^{-1}\| \geqslant \epsilon^{-1}\} \tag{49}$$

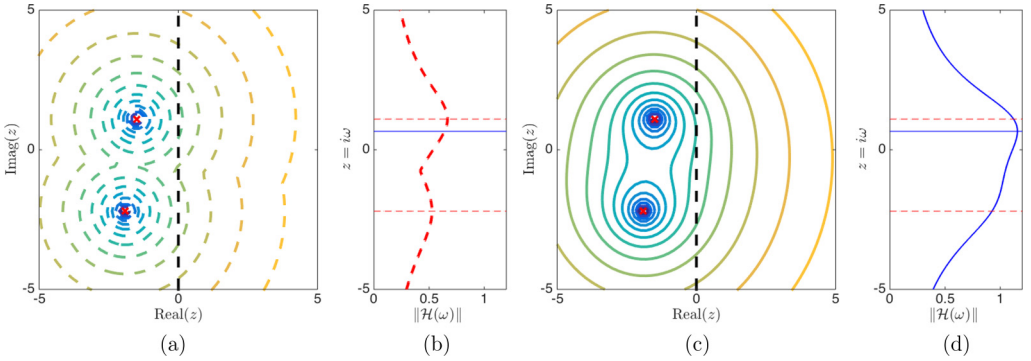

FIG. 2. Comparison of the pseudospectra and resolvent norm for the operators given in Eqs. (47) and (48), which have the same eigenvalues: (a), (b) normal operator $\boldsymbol{S}$ and (c), (d) non-normal operator $\boldsymbol{P}$. The eigenvalues, i.e., the eigenspectra, are marked by red crosses and color contours outline the bounds of the perturbed spectrum for constant perturbation magnitudes in (a), (c). The dashed contours in (a) reflect that the pseudospectra are circles centered on the eigenvalues, which is not true for the non-normal operator in (c). The resolvent norm in each case (b), (d) reflects the value of these contours along the imaginary axis. Dashed red horizontal lines indicate the resonant frequencies of the operator, i.e., the frequencies corresponding to the eigenvalues, while the solid blue horizontal line represents the most highly amplified frequency in the non-normal case.

and

$$\Lambda_\epsilon(\boldsymbol{P}) = \{z \in \mathbb{C} : \|(z\boldsymbol{I} - \boldsymbol{P})^{-1}\| \geqslant \epsilon^{-1}\}, \tag{50}$$

respectively.

For a normal operator such as $\boldsymbol{S}$, $\kappa = 1$ and the level curves of ϵ are proportional to the distance from the closest eigenvalue. The resolvent norm for a particular ω is inversely proportional to the distance from $i\omega$ to the nearest eigenvalue. This is what we refer to as the resonance curve. The spectrum and pseudospectra of $\boldsymbol{S}$ are shown in Fig. 2(a); there are two stable eigenvalues denoted by red crosses, and the pseudospectra consist of circular contours centered on the two eigenvalues. Since both eigenvalues are significantly damped, amplification due to resonance is not possible and the magnitude of the resolvent norm is less than 1 [Fig. 2(b)]. Moreover, the eigenvalue and singular value decompositions of $\boldsymbol{S}$ yield parallel basis functions, and the singular values are simply the magnitude of the eigenvalues.

Operator $\boldsymbol{P}$, however, is non-normal due to the nonzero off-diagonal term and, with reference to Eq. (25), $\kappa > 1$. The shifts of the eigenvalues of the perturbed operator are not proportional to ϵ, as indicated by the pseudospectrum isocontours in Fig. 2(c), and the resolvent norm of Fig. 2(d) is appreciably larger than that of the normal case in Fig. 2(a), with values exceeding 1. Furthermore, the maximum value of the resolvent norm occurs at a nonresonant frequency, $\omega = 0.66$. Amplification is possible for a linearly stable operator due to pseudoresonance under forcing at any frequency for which $\|\mathcal{H}(\omega)\| > 1$. It is important to add that even when the primary contribution to amplification is a normal mechanism, non-normality can still contribute to exacerbate the response. For example, the amplification at the frequencies of the eigenvalues in Fig. 2 is higher for operator $\boldsymbol{P}$ than it is for the purely normal operator $\boldsymbol{S}$. That being the case, the right-hand side of Eq. (25) may be large due to one or both terms in the product.

E. Projection of resolvent modes onto eigenmodes

The projections of the first resolvent mode $\hat{\boldsymbol{\psi}}_1$ onto the eigenvectors of operators $\boldsymbol{P}$ and $\boldsymbol{S}$ are plotted in Fig. 3 for various ω. For $\boldsymbol{S}$, the values are either one or zero, meaning that $\hat{\boldsymbol{\psi}}_1$ is one of the operator's eigenvectors, even at nonresonant frequencies. The eigenvector it chooses is simply whichever eigenvalue is closest to $z = i\omega$ for a given ω. The projections for operator $\boldsymbol{P}$ are far more

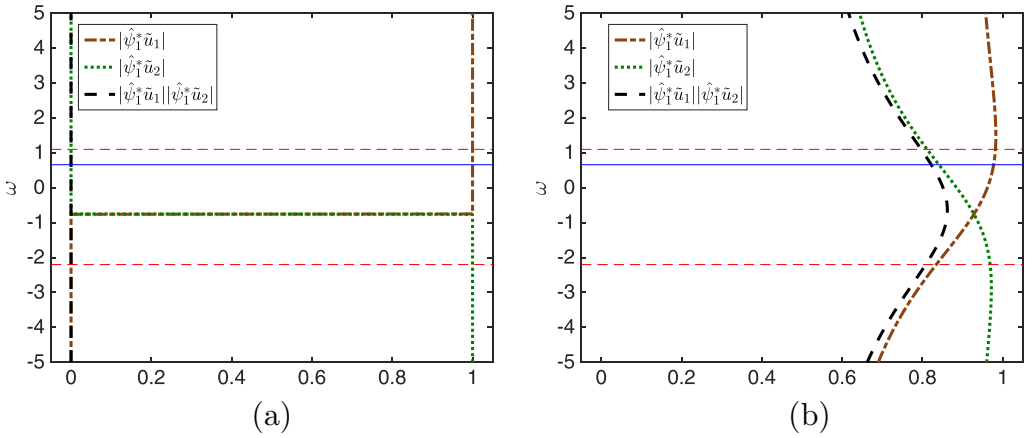

FIG. 3. Projection of the first resolvent mode $\hat{\boldsymbol{\psi}}_1$ onto the eigenvectors $\tilde{\boldsymbol{u}}_1$ (dash-dotted brown line) and $\tilde{\boldsymbol{u}}_2$ (dotted green line) of (a) $\boldsymbol{S}$ and (b) $\boldsymbol{P}$. The product of these projections is the long-dashed black line. Dashed red horizontal lines indicate the resonant frequencies of the operators and the solid blue horizontal line represents the most highly amplified frequency in the non-normal case.

interesting. There is a nontrivial projection of $\hat{\boldsymbol{\psi}}_1$ onto both eigenvectors for every ω, hence why the resolvent norm in Fig. 2 is higher for operator $\boldsymbol{P}$ at every frequency. The maximum $|\hat{\boldsymbol{\psi}}_1^* \tilde{\boldsymbol{u}}_1|$ and $|\hat{\boldsymbol{\psi}}_1^* \tilde{\boldsymbol{u}}_2|$ occur at λ_1 and λ_2, respectively, which is to be expected since the forcing is at the frequency of these eigenvalues. The projections at the most amplified frequency ($\omega = 0.66$) are both high, which can be seen by their product. The frequency where the product peaks, however, does not match the most amplified frequency since $\mathrm{Real}(\lambda_1) < \mathrm{Real}(\lambda_2)$, hence the resolvent's preference for choosing a frequency closer to λ_1.

Since both eigenvectors are needed to capture the behavior of operator $\boldsymbol{P}$ but only one resolvent mode is needed, it can be concluded that resolvent modes are a more efficient basis for capturing the dominant input-output behavior of the operator. It can also be inferred that the projection of $\hat{\boldsymbol{\psi}}_2$ onto the eigenvectors is relatively small since it is orthogonal to $\hat{\boldsymbol{\psi}}_1$. It is no surprise, therefore, that the resolvent operator tends to be low rank at pseudoresonant frequencies since the optimal resolvent response mode projects onto many eigenvectors. This forces suboptimal resolvent modes to be nearly orthogonal to many eigenvectors of the LNS operator and so their contribution to the input-output behavior is negligible.

Having examined the implications of the structure of the operator on amplification and forcing and response modes, we now consider two real example flows. Low Reynolds number cylinder flow is used to investigate the choice of base or mean flow as the linear stability threshold is crossed (Sec. IV). A canonical wall turbulence configuration is employed to identify the influence of the various terms in the resolvent on the resulting SVD (Sec. V).

IV. APPLICATION TO CYLINDER FLOW

We apply a global resolvent analysis to the base and mean velocity profiles for cylinder flows under the critical Reynolds number $\mathrm{Re}_c \leqslant 47$ [7–9], as well as mean flows of the two-dimensional (2D) laminar vortex shedding regime where $\mathrm{Re} \leqslant 189$ [49]. Cylinder flow is a particularly suitable choice to investigate trends associated with the wavemaker since it exhibits a region of absolute instability.

A. Numerical methods

The relevant procedures for computing the two-dimensional base and mean flows, $\boldsymbol{U}_0$ and $\overline{\boldsymbol{u}}$, are detailed here before applying the analysis tools.

The NSEs [Eq. (1)] are nondimensionalized by the cylinder diameter D and inlet velocity U_∞, which are both set to unity. For the base flow calculation, a uniform inlet velocity condition is prescribed while no-slip Dirichlet boundary conditions are applied to the cylinder surface, symmetric conditions to the upper and lower boundaries, and advective conditions to the outlet. The nonlinear equations for $\boldsymbol{U}_0$ are solved using a Newton method on a finite-element mesh generated by FREEFEM++ (see [50]). Taylor-Hood finite elements (P1b, P1b, P1 for U_0, V_0, and P_0, respectively) are used for spatial discretizations. The computational domain Ω spans $-30 \leqslant x/D \leqslant 60$, $-25 \leqslant y/D \leqslant 25$ with the cylinder centered at the origin and the mesh is made up of 104 214 triangles resulting in 365 358 degrees of freedom for velocity and pressure.

A DNS of the cylinder flow is also performed to obtain the mean flow profile using FREEFEM++ with the same boundary conditions and mesh. A second-order semi-implicit time discretization is employed with a nondimensional time step $\Delta t = 0.02$. Beyond Re_c, the simulated flow settles into regular vortex shedding at a fixed amplitude A and temporal frequency ω_s where the subscript s denotes shedding. The mean flow $\overline{\boldsymbol{u}}$ is computed by time-averaging the DNS state vector over 25 complete shedding cycles. The linear operators are formed in FREEFEM++ and the only boundary condition which differs with respect to the base flow calculation is at the inlet where homogeneous boundary conditions are enforced so that the perturbations vanish at infinity. The eigenvalues are computed using a shift-and-invert strategy, the details of which are discussed in Nayar and Ortega [51]. The generalized eigenvalue problem is then solved with the implicitly restarted Arnoldi method using the ARPACK library developed by Lehoucq and Sorensen [52].

The singular values of the resolvent operator are computed in a manner outlined by Sipp and Marquet [53]; a brief summary of the procedure is presented here. The singular value problem is reformulated as the following eigenvalue problem:

$$\mathcal{H}(\omega)^*\mathcal{H}(\omega)\hat{\boldsymbol{\phi}}_i = \sigma_i^2\hat{\boldsymbol{\phi}}_i, \tag{51}$$

where $\hat{\boldsymbol{\phi}}_i$ is the ith right singular vector corresponding to the singular value σ_i of $\mathcal{H}(\omega)$. The largest eigenvalues of the Hermitian operator $\mathcal{H}(\omega)^*\mathcal{H}(\omega)$ are computed using the ARPACK library and the parallel MUMPS solver developed by [54]. The response modes are then computed from Eq. (16).

B. Base flow velocity profile

A resolvent analysis is performed on the cylinder base flow for various Reynolds numbers over a range of ω. Contours of the pseudospectrum for $\mathrm{Re} = 47$ are overlaid onto the spectrum, which is in agreement with Sipp and Lebedev [10] to within the sensitivity to the mesh geometry, in Fig. 4(a). The variation of the resolvent norm along the imaginary axis, i.e., σ_1, is plotted alongside the second singular value of the resolvent, σ_2, and the resonance curve in Fig. 4(b). There is a frequency $\omega_{\max}$ where the first singular value is several orders of magnitude larger than all the others (only two are shown for clarity). The least stable eigenvalue, whose imaginary part is $\omega_{\max}$, dominates the behavior of the resolvent norm and its influence spans from $0 < \omega < 1.1$. For the cylinder base flow at $\mathrm{Re} = 47$, $\omega_{\max} = 0.742$ corresponds to the true ω_s at the onset of vortex shedding. The amplification is significantly lower for all other frequencies, including harmonics, and the resolvent is not low rank since the eigenvalues are not separated for $\omega > 1.1$. This lack of a low-rank behavior has also been observed, for example, in jet flow by Schmidt *et al.* [21].

The previous observations reinforce why stability analysis about the base flow can predict Re_c. Only one structure at the globally most amplified frequency is prone to significant amplification at subcritical Reynolds numbers and it is the first to become unstable. This is characteristic of an absolute instability mechanism in which frequency selection is not influenced by background noise. The stability modes and resolvent modes are nearly identical as seen in Fig. 5. The effect of lift-up is weak since the energy is fairly evenly distributed in the u and v components of both the forcing and response modes in Fig. 5. Mean flow advection, on the other hand, plays a significant role in the spatial support of the forcing and response modes which are located upstream and downstream of the cylinder. Chomaz [26] made an analogous observation for the forward and adjoint eigenmodes

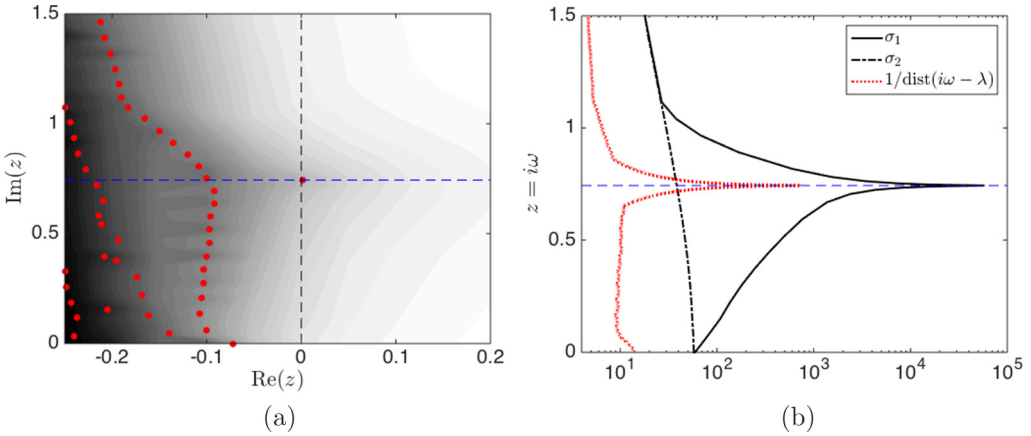

FIG. 4. (a) Spectrum (red dots) and pseudospectrum (solid contours, ϵ increasing as colors change from dark to light) of the LNS operator for the cylinder base flow at Re = 47. (b) The resolvent norm, σ_1 (solid line), i.e., the value of ϵ^{-1} along the imaginary axis, second largest singular value σ_2 (dash-dotted line), and inverse distance from the imaginary axis to the nearest eigenvalue (dotted red line).

and attributed this to convective non-normality. Since the resolvent operator is low rank, computing $|\hat{\boldsymbol{\phi}}_1^* \hat{\boldsymbol{\psi}}_1|^{-1}$ is a good estimate of the non-normal amplification experienced by the flow. We obtain a value of $\|\hat{\boldsymbol{\phi}}_1^* \hat{\boldsymbol{\psi}}_1\|^{-1} = 79.4$ which is in good agreement with $\sigma_1(\omega_{\max})|i\omega_{\max} - \lambda_{\mathrm{ls}}| = 79.3$ (see Table II). This accounts for the large gap between the peaks of the resolvent norm and resonance curve in Fig. 4(b).

The least stable global mode and its adjoint counterpart are computed for various Reynolds numbers near and below Re_c to illustrate the cylinder transition from convective to absolute instability. Figure 6 juxtaposes the v component of the adjoint mode, forward mode, and wavemaker. The forward mode has unit magnitude while the adjoint mode has been normalized with respect to the forward mode such that their inner product is unity. A wavemaker first appears for Re = 25, the Reynolds number at which Monkewitz [30] determined the cylinder wake is absolutely unstable. There is no wavemaker for lower Reynolds numbers due to the downstream location of the forward eigenmode which is a consequence of mean flow advection; the strength of the reverse flow is not sufficient to produce an overlap region. For the lowest two Reynolds numbers considered in Fig. 6, the contour levels of the forward eigenmode immediately behind the cylinder are three orders of magnitude smaller than their higher Reynolds number counterparts. The downstream location where the contour levels are significant does not appear within the plotted domain. As the Reynolds number increases, the velocity deficit grows and the reverse flow directly behind the cylinder strengthens. The forward eigenmode gradually appears closer to the cylinder until there is a nontrivial overlap between it and its adjoint counterpart.

TABLE II. Quantification of non-normality for the most amplified modes in cylinder and turbulent channel flows.

	$\boldsymbol{k}$ or ω	σ_1	$\lvert i\omega - \lambda\rvert^{-1}$	$\sigma_1 \lvert i\omega - \lambda\rvert$	$\lvert\hat{\boldsymbol{\phi}}_1^* \hat{\boldsymbol{\psi}}_1\rvert^{-1}$
Cylinder base	$\omega = 0.743$	5.78×10^4	729	79.3	79.4
Cylinder mean	$\omega = 1.02$	1.65×10^4	570	28.9	26.9
Near-wall cycle	$(k_x,k_z,c^+) = (4\pi,40\pi,14)$	0.502	2.56×10^{-2}	19.6	4.81
VLSM	$(k_x,k_z,c^+) = (\pi/9,2\pi/3,22)$	479	3.28	146	34.9
Stationary disturbance	$(k_x,k_z,\omega) = (0,2\pi/3,0)$	8.14×10^4	293	278	250

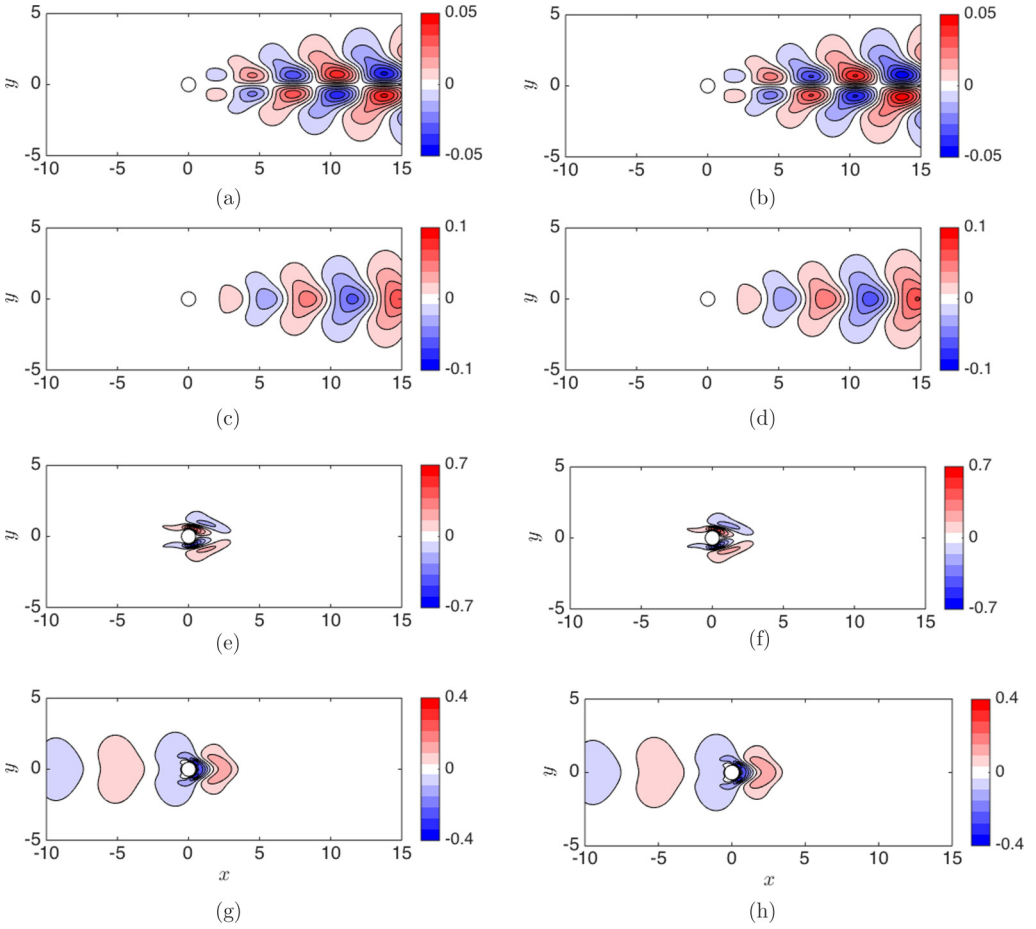

FIG. 5. Comparison of stability modes (left) with resolvent modes (right) at the critical Reynolds number $\mathrm{Re}_c = 47$ and a temporal frequency of $\omega = 0.742$: (a), (b) streamwise component of the forward or response mode, (c), (d) transverse component of the forward or response mode, (e), (f) streamwise component of the adjoint or forcing mode, and (g), (h) transverse component of the adjoint or forcing mode. The eigenmodes and resolvent mode shapes are essentially indistinguishable for this flow.

Beyond the critical Reynolds number, the region of the flow which is absolutely unstable is sufficiently long for the flow to become globally unstable. Perturbations grow exponentially in time until they are saturated by nonlinearities. The resulting velocity fluctuations are dominated by the vortex shedding. Once the flow has reached a limit cycle, the shedding frequency is different from that predicted by resolvent analysis of the base flow since the frequency of the least stable perturbations is altered during the saturation process. Additionally, the mean recirculation region behind the cylinder is shorter than its base flow counterpart in the streamwise direction.

C. Mean velocity profile

The focus of resolvent analysis typically shifts when using the mean velocity profile rather than the base flow. The goal becomes identification of the energetically important structures and their frequencies in the unsteady flow rather than prediction of the external forcing and structure which appears when the flow becomes unsteady.

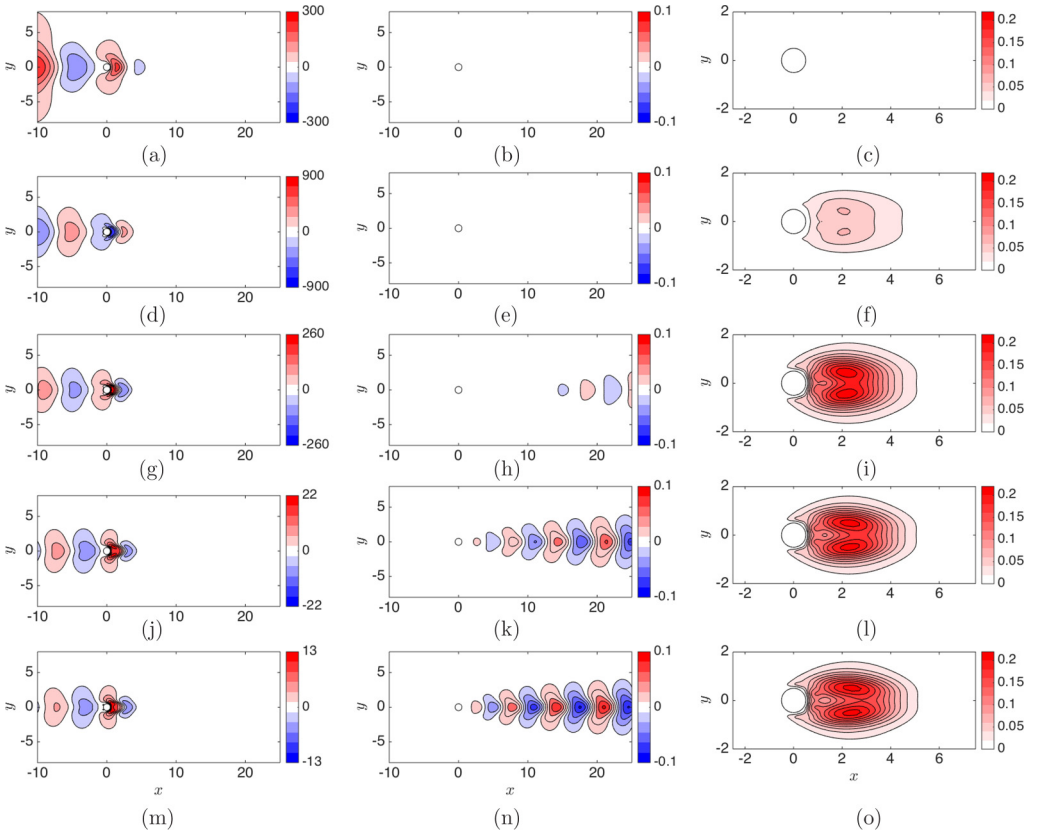

FIG. 6. Contours of the transverse velocity for the leading adjoint modes $\tilde{v}^{\dagger}$ (left) and forward modes $\tilde{v}$ (middle) of the base flow. The Reynolds numbers (Re = 15, 25, 35, 45, and 50) increase from top to bottom. The wavemaker $\mathcal{W}$ (right) is computed using the forward and adjoint modes. Contour levels are not identical for the adjoint modes which are normalized based on the forward modes. Note that the streamwise velocity component has not been plotted even though the wavemaker depends on this quantity.

Contours of the pseudospectrum corresponding to the mean flow in the 2D laminar shedding regime are overlaid with the spectrum of the mean flow at Re = 100 in Fig. 7. The resolvent norm along the imaginary axis is plotted alongside the second largest singular value and resonance curve. Similar to the base flow, there is only one frequency at which there is a resonant peak. Unlike the base flow case, the most amplified frequency at supercritical Reynolds numbers correctly predicts the shedding frequency as seen in Fig. 8. While the resolvent norm always peaks at a distinct frequency for all cases, the growth rate of the least stable eigenvalue of the base flow continues to grow while the frequency remains roughly constant. Figure 8 shows that the largest peak occurs at the stability limit, Re_c. The maximum amplification, which is proportional to the inverse distance between the eigenvalue and the imaginary axis, indicates the progression of the least stable pole across the complex plane and over the imaginary axis. The resolvent norm has not been plotted for supercritical base flows since the resolvent attempts to quantify the size of perturbation necessary for the spectrum to cross the neutral axis. For the base flow at the critical Reynolds number Re_c and mean flows where $\mathrm{Re} > \mathrm{Re}_c$, the size of this perturbation is very small, leading to very highly amplified disturbances.

The peak resolvent norm for the mean flows has no discernible pattern in Fig. 8 since the real part of the eigenvalue is approximately zero. It is very sensitive, therefore, to the spatial resolution and temporal convergence of the mean flow in addition to the discretization of ω. Nevertheless, proportionality between the resolvent and stability mode shapes can be expected. Substituting $i\omega_s$

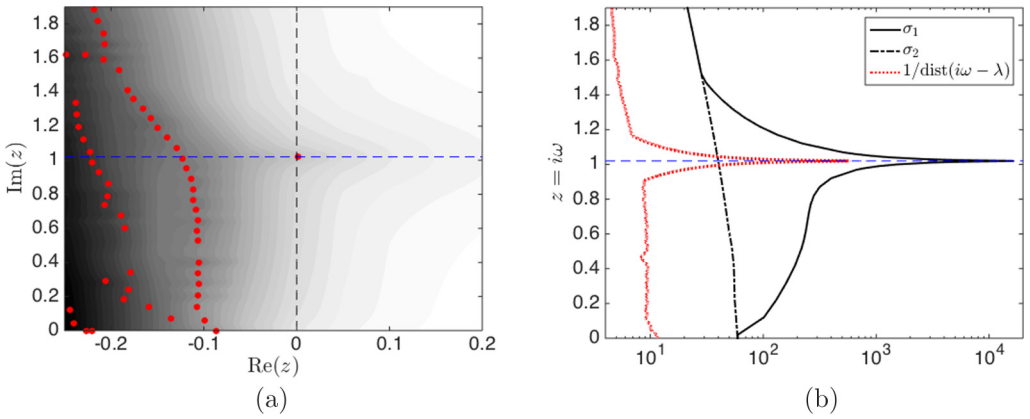

FIG. 7. (a) Spectrum (red dots) and pseudospectrum (solid contours, ϵ increasing as colors change from dark to light) of the LNS operator for the cylinder mean flow at Re = 100. (b) The resolvent norm, σ_1 (solid line), i.e., the value of ϵ^{-1} along the imaginary axis, second largest singular value σ_2 (dash-dotted line), and inverse distance from the imaginary axis to the nearest eigenvalue (dotted red line).

for λ into Eq. (31), since the real part of the marginally stable mode is nearly zero, yields

$$\mathcal{H}(\omega_s) \approx \tilde{\boldsymbol{u}}_s \tilde{\boldsymbol{v}}_s^* \approx \hat{\boldsymbol{\psi}}_s \hat{\boldsymbol{\phi}}_s^*. \tag{52}$$

The sum in Eq. (31) is dominated by the contribution from the marginally stable mode so the resolvent operator can be approximated by the outer product of the marginally stable mode and its adjoint counterpart or the optimal resolvent response and forcing modes at ω_s. Similar to the base flow case, we can quantify $|\hat{\boldsymbol{\phi}}_1^* \hat{\boldsymbol{\psi}}_1|^{-1} = 26.9$ and this agrees fairly well with the ratio of $\sigma_1(\omega_s)|i\omega_s - \lambda_s| = 28.9$ (see Table II).

Rather than comparing the stability and resolvent mode shapes as shown in Fig. 5, the contribution of the fluctuating feedback force to the wavemaker (see [44]) for Re = 100 is computed using stability and resolvent modes in Figs. 9(a) and 9(b), respectively. Figure 9(a) is in good agreement with Meliga *et al.* [44] and the agreement between Figs. 9(a) and 9(b) is excellent, implying that the underlying modes are indeed proportional to each other. Streamlines from the mean flow are superimposed to observe how the wavemaker is related to the mean recirculation bubble, the size of which depends

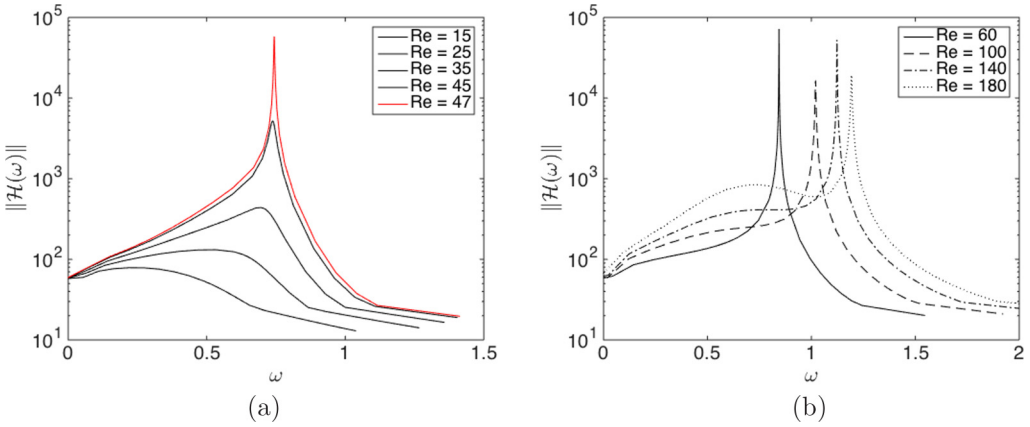

FIG. 8. (a) The resolvent norm for the critical (solid red line) and subcritical (solid black lines) base flows. (b) The resolvent norm for supercritical mean flows.

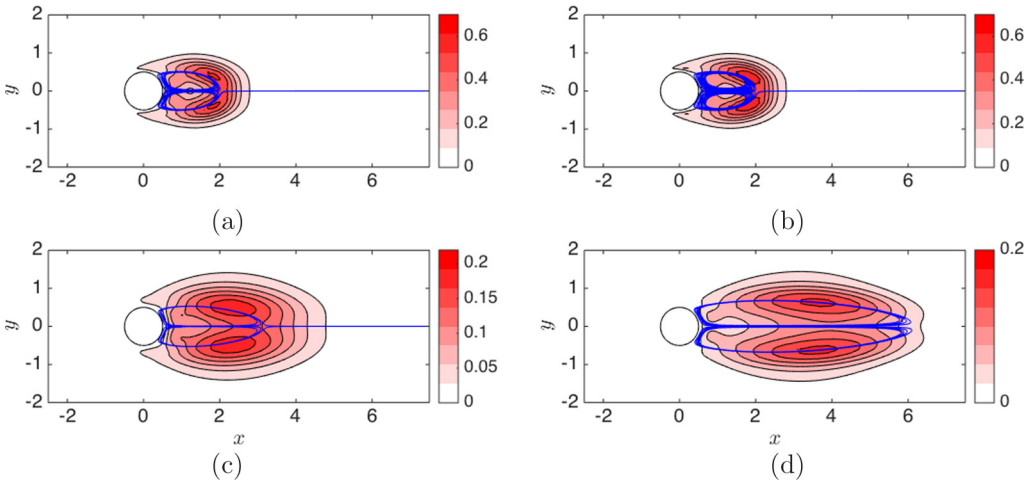

FIG. 9. Wavemakers for mean flow at $\mathrm{Re} = 100$ computed from (a) stability modes and (b) resolvent modes. Wavemakers for the base flow at (c) $\mathrm{Re} = 47$ and (d) $\mathrm{Re} = 100$. Blue lines superimpose the mean flow streamlines which delineate the mean recirculation bubble.

on Reynolds number. The length of the recirculation bubble scales with the streamwise extent of the wavemaker region for any Reynolds number for either the mean flow as seen in Figs. 9(a) and 9(b) or the base flow as seen in Figs. 9(c) and 9(d). The wavemaker regions associated with the base profile are shown in Figs. 9(c) and 9(d) for $\mathrm{Re} = 47$ and $\mathrm{Re} = 100$, respectively. Figures 9(a) and 9(d) compare the mean and base wavemakers at $\mathrm{Re} = 100$, the main difference being that, as the Reynolds number increases, both the mean recirculation bubble [55] and the wavemaker region shrink. For the unstable base flows, increasing the Reynolds number will also increase the streamwise length of the recirculation bubble and wavemaker region as seen in Figs. 9(c) and 9(d).

V. APPLICATION TO WALL TURBULENCE

We now consider turbulent channel flow in the context of the discussion from Sec. III. Unlike the cylinder flow, which is an oscillator with intrinsic dynamics that are insensitive to background noise, this flow is an example of a noise amplifier; as such, pseudoresonance plays a big role and leads to significant amplification at nonresonant frequencies. Due to its geometric simplicity, we choose channel flow at $\mathrm{Re}_\tau = 2000$ which has a parallel mean velocity profile $\overline{\boldsymbol{u}} = \overline{u}(y)$.

A. Numerical methods

We again consider the nondimensional, incompressible NSEs where the channel half height h and the friction velocity $u_\tau = \sqrt{\tau_w/\rho}$ (where τ_w is the wall shear stress, ρ is the density) are the characteristic scales to obtain

$$\partial_t \boldsymbol{u} + \boldsymbol{u} \cdot \nabla \boldsymbol{u} = -\nabla p + \mathrm{Re}_\tau{}^{-1} \nabla^2 \boldsymbol{u}, \tag{53a}$$

$$\nabla \cdot \boldsymbol{u} = 0, \tag{53b}$$

where $\mathrm{Re}_\tau = h u_\tau / \nu$ and ν is the kinematic viscosity. The streamwise direction and spanwise directions are periodic, and the wall-normal domain extends from $y/h = -1$ to $y/h = 1$ with no-slip and no-penetration conditions imposed at the wall. The velocity field is Reynolds decomposed into

the sum of a spatiotemporal mean and fluctuations,

$$\boldsymbol{u}(x,y,z,t) = \overline{u}(y) + \boldsymbol{u}'(x,y,z,t). \tag{54}$$

Here we assume the mean velocity profile is known *a priori* from an eddy viscosity model [35] as discussed in [38]. We express the fluctuations as Fourier modes in the streamwise and spanwise directions and in time,

$$\hat{\boldsymbol{u}}(k_x,k_z,\omega;y) = \int_{-\infty}^{\infty}\int_{-\infty}^{\infty}\int_{-\infty}^{\infty} \boldsymbol{u}'(x,y,z,t)e^{-i(k_x x+k_z z-\omega t)}dx\,dz\,dt, \tag{55}$$

where k_x is the streamwise wavenumber, k_z is the spanwise wavenumber, and ω is the radial frequency. Upon elimination of the pressure term, we can express the governing equations in terms of the fluctuating vertical velocity $\hat{v}$ and normal vorticity $\hat{\eta} = ik_z\hat{u} - ik_x\hat{w}$,

$$-i\omega\begin{pmatrix}\hat{v}\\ \hat{\eta}\end{pmatrix} + \begin{pmatrix}k^2-\mathcal{D}^2 & 0\\ 0 & 1\end{pmatrix}^{-1}\begin{pmatrix}\mathcal{L}_{OS} & 0\\ ik_z\overline{u}' & \mathcal{L}_{SQ}\end{pmatrix}\begin{pmatrix}\hat{v}\\ \hat{\eta}\end{pmatrix} = \boldsymbol{J}\hat{\boldsymbol{f}}, \tag{56}$$

where the Orr-Sommerfeld (OS) and Squire (SQ) operators are given by

$$\mathcal{L}_{OS} = ik_x\overline{u}(k^2-\mathcal{D}^2) + ik_x\overline{u}'' + \frac{1}{\mathrm{Re}_\tau}(k^2-\mathcal{D}^2)^2, \tag{57}$$

$$\mathcal{L}_{SQ} = ik_x\overline{u} + \frac{1}{\mathrm{Re}_\tau}(k^2-\mathcal{D}^2), \tag{58}$$

and

$$\boldsymbol{J} = \begin{pmatrix}k^2-\mathcal{D}^2 & 0\\ 0 & 1\end{pmatrix}^{-1}\begin{pmatrix}-ik_x\mathcal{D} & -k^2 & -ik_z\mathcal{D}\\ ik_z & 0 & -ik_x\end{pmatrix}, \tag{59}$$

$$\hat{\boldsymbol{f}} = \begin{pmatrix}\hat{f}_u\\ \hat{f}_v\\ \hat{f}_w\end{pmatrix} = -\langle\boldsymbol{u}'\cdot\nabla\boldsymbol{u}'\rangle_{\boldsymbol{k}}. \tag{60}$$

Here $\mathcal{D} = \frac{\partial}{\partial y}$, $k^2 = k_x^2 + k_z^2$, and $\langle\,\rangle_{\boldsymbol{k}}$ denotes the Fourier component associated with the wavenumber vector $\boldsymbol{k} = (k_x,k_z,\omega)$. The wall-normal operators are discretized numerically with Chebyshev collocation points using the suite developed by [56]. We can recast Eq. (56) into the following input-output form:

$$\begin{pmatrix}\hat{u}\\ \hat{v}\\ \hat{w}\end{pmatrix} = \mathcal{H}(k_x,k_z,\omega)\begin{pmatrix}\hat{f}_u\\ \hat{f}_v\\ \hat{f}_w\end{pmatrix}, \tag{61}$$

where the resolvent operator $\mathcal{H}$ is given by

$$\mathcal{H}(k_x,k_z,\omega) = \boldsymbol{K}(-i\omega + \boldsymbol{L})^{-1}\boldsymbol{J}, \tag{62}$$

where

$$\boldsymbol{L} = \boldsymbol{G}^{-1}\mathcal{L}, \tag{63}$$

$$\boldsymbol{G} = \begin{pmatrix}k^2-\mathcal{D}^2 & 0\\ 0 & 1\end{pmatrix}, \tag{64}$$

$$\mathcal{L} = \begin{pmatrix}\mathcal{L}_{OS} & 0\\ ik_z\overline{u}' & \mathcal{L}_{SQ}\end{pmatrix}, \tag{65}$$

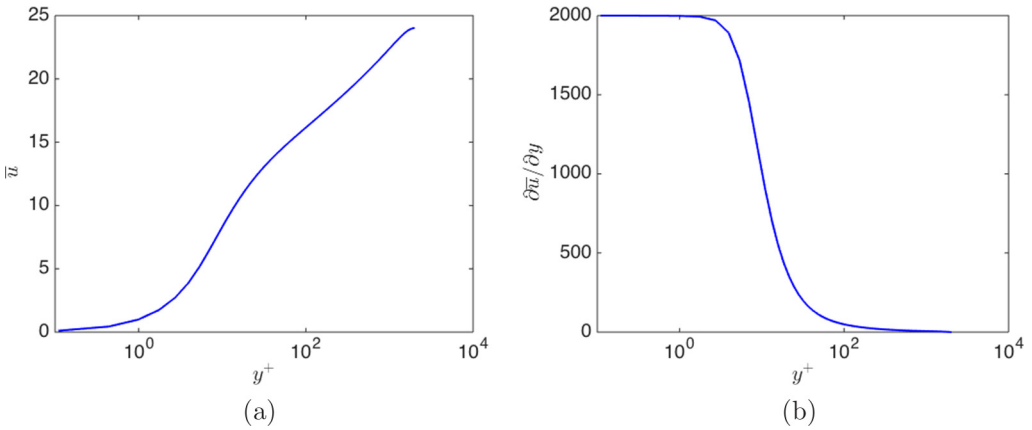

FIG. 10. (a) Turbulent mean velocity profile for channel flow at $\mathrm{Re}_\tau = 2000$ plotted in inner units alongside (b) the mean shear.

$$\boldsymbol{K} = \frac{1}{k^2}\begin{pmatrix} ik_x\mathcal{D} & -ik_z \\ k^2 & 0 \\ ik_z\mathcal{D} & ik_x \end{pmatrix}. \tag{66}$$

As before, we can decompose the resolvent operator via the SVD as

$$\mathcal{H}(k_x,k_z,\omega) = \boldsymbol{\Psi}(k_x,k_z,\omega)\boldsymbol{\Sigma}(k_x,k_z,\omega)\boldsymbol{\Phi}^*(k_x,k_z,\omega). \tag{67}$$

The off-diagonal term in $\boldsymbol{L}$ is proportional to the mean shear $\overline{u}'$ which is maximum at the wall. It remains large in the inner region before it begins to decline in the logarithmic region. Similar to the model LNS operator in Sec. III, mean shear is the primary source of non-normality leading to significant amplification. Its spatial variation is important since it has been shown [17] that a critical-layer mechanism tends to localize activity at the wall-normal location where the phase speed of the disturbance is equal to the local mean velocity. This is explored further by considering three particular wavenumber triplets that are representative of the near-wall cycle, a very large-scale motion (VLSM), and a stationary disturbance. The roles of normal and non-normal mechanisms are studied by analyzing the mode shapes of the leading resolvent response modes, the pseudospectrum of the LNS operator, and the resolvent norm compared with the resonance curve.

B. Near-wall cycle

The first wavenumber combination considered is $(k_x,k_z,c^+) = (4\pi,40\pi,14)$ which is representative of the near-wall cycle [17]. Here the wave speed is given by $c^+ = \omega/k_x$. This choice of wave speed, which is slightly larger than the typically quoted value of $c^+ = 10$ for the near-wall cycle, corresponds to the largest resolvent norm. However, it should be noted that the ensuing arguments are insensitive to this small discrepancy, with the main quantitative difference arising in the wall-normal location where the modes are localized. Figure 10 shows that the mean shear is very large at the wall-normal height where the wave speed matches the local mean, resulting in the off-diagonal terms of the resolvent operator being large. This is similar to the model LNS operator in Eq. (45) where the influence of non-normality concentrates energy in different velocity components for $\hat{\boldsymbol{\psi}}_1$ and $\hat{\boldsymbol{\phi}}_1$. The optimal resolvent forcing and response modes are plotted in Fig. 11 to illustrate that the forcing is primarily concentrated in v and w while the response is mostly in u.

The strength of mean shear suggests that pseudoresonance is the primary driver of the near-wall cycle mode. The spectrum as well as contours of the pseudospectrum are plotted in Fig. 12 for various ϵ. Figure 12 also includes the resolvent norm and resonance curve. The ratio of the resolvent norm to the contribution from resonance is 19.6, which is of the same order of magnitude as the

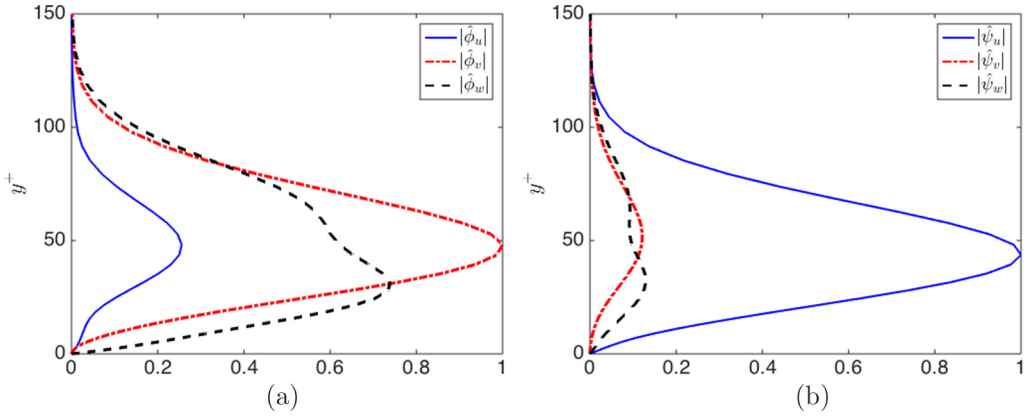

FIG. 11. Velocity amplitudes for (a) the optimal forcing mode $\hat{\boldsymbol{\phi}}_1$ and (b) the optimal response mode $\hat{\boldsymbol{\psi}}_1$ corresponding to the wavenumber triplet of $(k_x,k_z,c^+) = (4\pi,40\pi,14)$.

value predicted by $|\hat{\boldsymbol{\phi}}_1^* \hat{\boldsymbol{\psi}}_1|^{-1} = 4.81$ (see Table II). Nevertheless, it is clear from this discrepancy that amplification cannot be attributed to one particular eigenvalue and that there is no eigenvector which is proportional to the resolvent mode. Using the expression $\sigma_1|i\omega - \lambda|$ to quantify non-normality is problematic since there is no unique λ which is responsible for amplification.

The ω corresponding to $c^+ = 14$ is indicated by the horizontal, dashed blue line. At this frequency, the resolvent norm is significantly larger than the resonance term, suggesting that amplification is due to non-normal mechanisms. This observation is confirmed by the spectrum where the least damped eigenvalues are clustered around higher frequencies and contribute to the resolvent norm for $\omega > 300$. It is also worth noting that the eigenvalues are significantly damped, which results in the leading

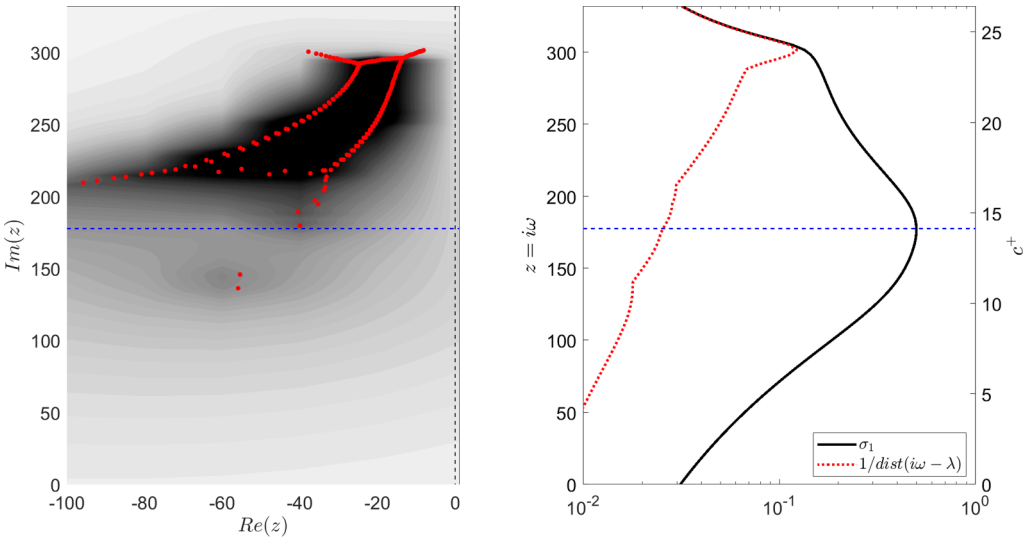

FIG. 12. The eigenvalues of the operator $\boldsymbol{L}(k_x = 4\pi,k_z = 40\pi)$ in red circles overlaid with contours of the pseudospectrum (left). The resolvent norm is plotted in the solid black line along with the inverse distance from the imaginary axis to the nearest eigenvalue, which is the dotted red line (right). The spatial wavenumbers correspond to the near-wall cycle, and the horizontal, dashed blue line represents the ω with the largest resolvent norm, which corresponds to a phase speed of $c^+ \approx 14$.

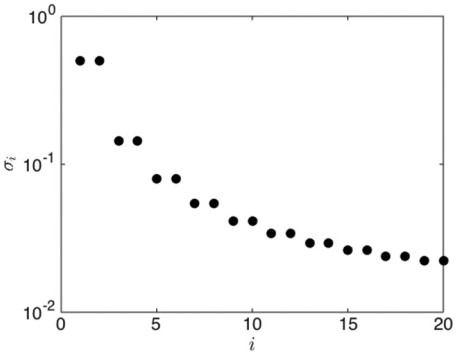

FIG. 13. First 20 singular values of the resolvent operator for $(k_x,k_z,c^+) = (4\pi,40\pi,14)$.

singular values being on the order of unity. While these are not large, the rank-1 approximation is still valid since the first pair of singular values is approximately one order of magnitude larger than the others as seen in Fig. 13.

C. VLSM

Further from the wall, the mean shear drops several orders of magnitude (see Fig. 10) and the effect of viscosity decreases. A wavenumber triplet which is representative of a VLSM is considered. The mode shapes for $(k_x,k_z,c^+) = (\pi/9,2\pi/3,22)$ are plotted in Fig. 14. The forcing is dominated by the w component while the response is dominated by the u component. The v component of the forcing, notably, is less significant than the near-wall cycle mode, implying that the role of lift-up is not as pronounced for this mode.

The spectrum associated with the streamwise and spanwise wavenumbers of the VLSM is plotted along with the pseudospectrum of the LNS operator in Fig. 15. The results are drastically different from the near-wall cycle case as the resonant forcing of eigenvalues is greater than 1 so amplification is due to both terms on the right-hand side of Eq. (25). Notably, the spectrum in Fig. 15 resembles that of the base flow at $\mathrm{Re} = 10\,000$ for $k_x = 1, k_z = 0$ as there are three distinct branches. As observed by Reddy *et al.* [22] and Schmid and Henningson [13], the eigenvalues at the intersection of the branches are the most sensitive to perturbations and result in very large non-normal amplification. The product

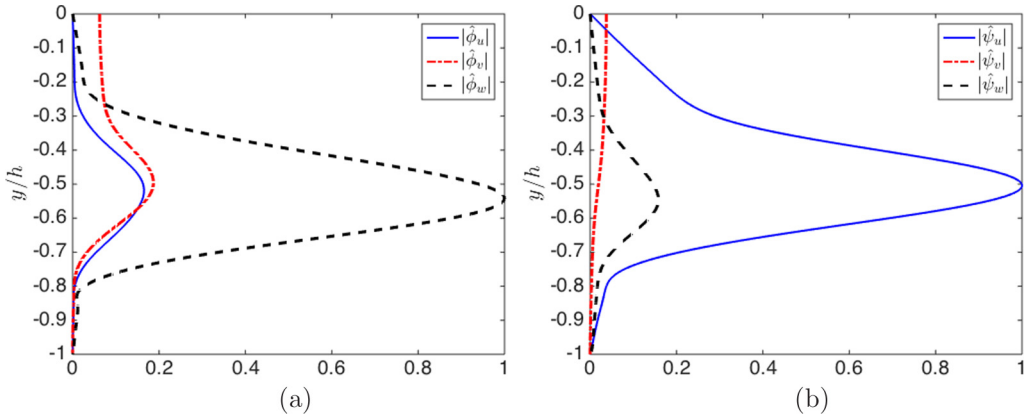

FIG. 14. Velocity amplitudes for (a) the optimal forcing mode $\hat{\boldsymbol{\phi}}_1$ and (b) the optimal response mode $\hat{\boldsymbol{\psi}}_1$ corresponding to the wavenumber triplet of $(k_x,k_z,c^+) = (\pi/9,2\pi/3,22)$.

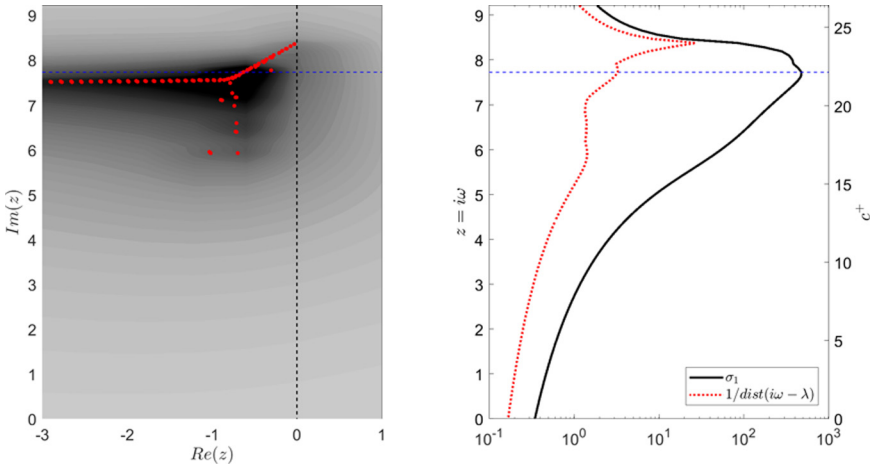

FIG. 15. The eigenvalues of the operator $\boldsymbol{L}(k_x = \pi/9, k_z = 2\pi/3)$ in red circles overlaid with contours of the pseudospectrum (left). The resolvent norm is plotted in the solid black line along with the inverse distance from the imaginary axis to the nearest eigenvalue, which is the dotted red line (right). The spatial wavenumbers correspond to the VLSM mode, and the horizontal, dashed blue line represents the ω with the largest resolvent norm, which corresponds to a phase speed of $c^+ \approx 22$.

$\sigma_1|i\omega - \lambda| = 146$ while $\|\hat{\boldsymbol{\phi}}_1^* \hat{\boldsymbol{\psi}}_1\|^{-1} = 34.9$ (see Table II), suggesting that the nonorthogonality of many eigenfunctions leads to high pseudoresonance. Similar to the near-wall cycle case, there are no eigenvalues which exactly match the wave speed associated with the VLSM. The eigenvalue close to the dotted blue line in Fig. 15, however, does seem to impact the resolvent norm which has an extra bump near its maximum value. This is also reflected in the dotted red line since the eigenvalue protrudes from the distinct Y shape of the spectrum. The maximum singular values are on the order of 10^3 and the resolvent operator is very low rank, as seen in Fig. 16.

D. Stationary disturbances

Finally, we consider stationary disturbances which tend to be the most amplified by the resolvent operator with singular values exceeding 10^4. The specific wavenumber triplet selected for this study is $(k_x, k_z, \omega) = (0, 2\pi/3, 0)$. The roots behind such large amplification can be traced back to the model operator in Eq. (45). In this example, $\partial\overline{u}/\partial y \to \infty$, resulting in a low-rank system which concentrated all the forcing energy in the second velocity component and the response energy in the first velocity

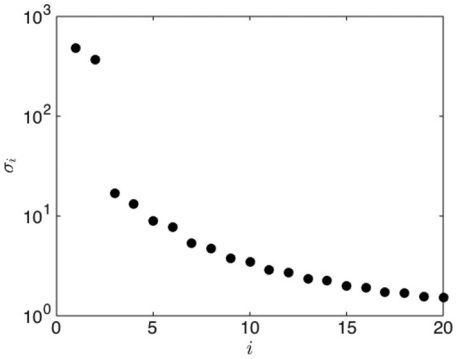

FIG. 16. First 20 singular values of the resolvent operator for $(k_x, k_z, c^+) = (\pi/9, 2\pi/3, 22)$.

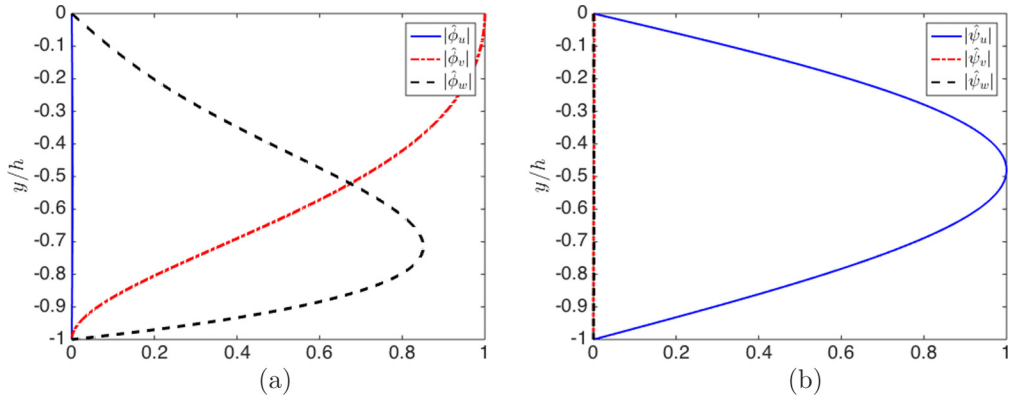

FIG. 17. Velocity amplitudes for (a) the optimal forcing mode $\hat{\boldsymbol{\phi}}_1$ and (b) the optimal response mode $\hat{\boldsymbol{\psi}}_1$ corresponding to the wavenumber triplet of $(k_x,k_z,\omega) = (0,2\pi/3,0)$.

component. When $k_x = \omega = 0$, all of the diagonal terms of the resolvent become order ϵ small since imaginary terms are eliminated and $\mathcal{D}$ scales with Re^{-1}. Thus, when the LNS operator is inverted, the determinant, which is the product of the diagonal terms, is very small. The energy for the forcing is almost totally in the wall-normal and spanwise components as seen in Fig. 17 while the response is almost totally in the streamwise component.

Similar to the near-wall cycle and VLSM modes, the spectrum and contours of the pseudospectrum are presented in Fig. 18 alongside the resolvent norm and contribution from resonance. All of the eigenvalues are real since the imaginary terms are eliminated from the resolvent operator when $k_x = 0$. Another implication of eliminating mean flow advection, as mentioned by [57], is that the Orr mechanism is absent from this mode. Stationary disturbances are highly amplified and the singular values are plotted in Fig. 19. The rank-1 approximation is quite applicable for this particular mode as the leading pair of singular values is on the order of 10^5. Moreover, the contribution of non-normality computed from $|\hat{\boldsymbol{\phi}}_1^* \hat{\boldsymbol{\psi}}_1|^{-1} = 250$, agrees quite well with $\sigma_1 |i\omega - \lambda| = 278$. Such agreement can be attributed to the eigenvalue closest to the imaginary axis which has an imaginary

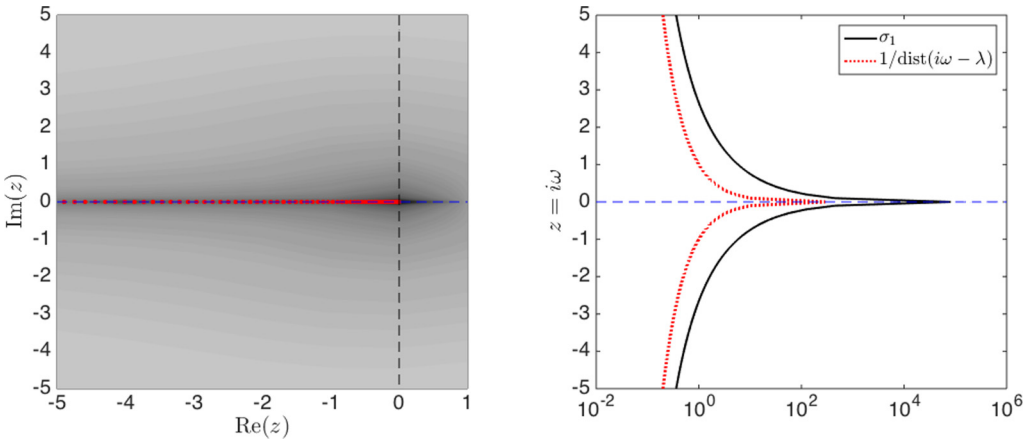

FIG. 18. The eigenvalues of the operator $\boldsymbol{L}(k_x = 0, k_z = 2\pi/3)$ in red circles overlaid with contours of the pseudospectrum (left). The resolvent norm is plotted in the solid black line along with the inverse distance from the imaginary axis to the nearest eigenvalue, which is the dotted red line (right). The horizontal, dashed blue line represents the ω corresponding to the phase speed of $c^+ = 0$.

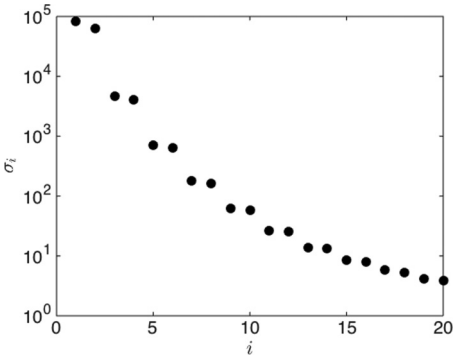

FIG. 19. First 20 singular values of the resolvent operator for $(k_x,k_z,\omega) = (0,2\pi/3,0)$.

component that agrees with the most amplified frequency. Unlike the cylinder case where there exists a convective-type non-normality, the $k_x = 0$ modes are an example of the component-type non-normality and so $|\hat{\boldsymbol{\phi}}_1^* \hat{\boldsymbol{\psi}}_1|$ is small since the velocity for the forcing mode is almost completely concentrated in the wall-normal plane while the velocity for the response mode is nearly all in the streamwise direction.

E. Influence of spatial wavenumber and wave speed

Based on the findings of this study and observations from [58], it is possible to categorize amplification mechanisms in wall-bounded turbulence as either normal or non-normal depending on the wavenumber vector $\boldsymbol{k}$ selected. When k_x is small, the influence of both mean flow advection and viscosity is diminished, resulting in a non-normal system where there is high amplification. Low-order modes (those corresponding to the largest singular values) experience high amplification due to both normality and non-normality. Higher-order modes also experience amplification due to non-normality. At higher k_x, only low-order modes are amplified as long as they are localized near the critical layer. Higher-order modes experience low amplification which is proportional to viscosity. The wall-normal height, furthermore, has implications on the type of amplification as it influences the choice of wave speed c, or ω, as well as the influence of mean shear $\partial\overline{u}/\partial y$. Closer to the wall, the mean shear is highest, while in the logarithmic region, mean shear still plays an important role resulting in preferential amplification of long streamwise structures.

VI. DISCUSSION AND CONCLUSIONS

We have juxtaposed stability and resolvent analyses and highlighted the types of amplification mechanisms they are likely to identify for flows in which linear mechanisms are important. The two can be formally related through a dyad expansion of the resolvent operator. When the resolvent identifies eigenmodes as the most amplified disturbance, the forward eigenmodes are proportional to the resolvent response modes and the adjoint eigenmodes are proportional to the resolvent forcing modes which, consequently, contain sensitivity information. This formulation also elucidates how to interpret the real part of eigenvalues belonging to the mean LNS operator. It plays a role in the degree to which a disturbance is amplified by the resolvent and it separates eigenvalues in the spectrum leading to low-rank behavior. This is particularly evident in cylinder flow, where the eigenvalue corresponding to the shedding mode is isolated from the other eigenvalues and is so close to the imaginary axis that it dominates the resolvent norm for a broad range of frequencies.

We have split the contributions to the resolvent norm into a resonance part and a non-normal part. The distance between the eigenvalue and a particular point on the imaginary axis quantifies the resonant contribution, and its product with the resolvent norm is one scalar measure of

non-normality. Non-normal amplification can also be computed by the inverse of the inner product between the most amplified resolvent forcing and response modes, i.e., $|\hat{\boldsymbol{\phi}}_1^* \hat{\boldsymbol{\psi}}_1|^{-1}$. If the two scalar measures of non-normality agree, it implies that amplification is due to a discrete eigenvalue and that the mean stability analysis is valid; otherwise, the amplification is due to pseudoresonance and $|\hat{\boldsymbol{\phi}}_1^* \hat{\boldsymbol{\psi}}_1|^{-1}$ is the best measure of non-normality. This also suggests that, to maximize the resolvent norm, it is desirable to minimize the overlap of the forcing and response modes, which biases the resolvent in favor of selecting amplification mechanisms which are as non-normal as possible.

Contours of the pseudospectrum have been overlaid with the spectrum for the mean LNS operator associated with cylinder and turbulent channel flow. It can be seen that the spectrum is very sensitive to perturbations in the latter flow due to high shear, which suggests that the least stable eigenvalues of the mean operator viewed in isolation are less informative than they are for the two-dimensional case. Moreover, the mode shapes and characteristics of the pseudospectrum can be predicted from the mean profile or wavenumber triad selected as they have implications for which terms in the LNS operator are most important.

These findings are applicable to both base and mean velocity profiles, but there is an important distinction. For a base flow, the input forcing must be provided by an external source. Therefore, the most amplified structure is of interest as it is likely to be present in the flow when it becomes unsteady. For a mean flow, the nonlinear term is the source of intrinsic forcing so the goal is to predict the structure of the unsteady flow [36]. In many cases, the most amplified response is normal in character and accounts for a significant amount of the kinetic energy of the velocity fluctuations (e.g., [5,59]). There are circumstances, however, where it does not give the complete picture as the rank-1 approximation is no longer valid and suboptimal modes need to be considered.

Cylinder flow is a case where resonance is the root of amplification leading to similarity of stability and resolvent modes. In both the base flow and mean flow cases, amplification occurs at a single frequency corresponding to the imaginary part of the least stable eigenvalue. The resolvent modes can be used to identify the wavemaker, which does not exist at very low Reynolds numbers when the flow is only convectively unstable. The cylinder exemplifies a convective-type non-normality where mean flow advection separates the spatial support of the forcing mode to be upstream of the response mode as long as $\overline{u} > 0$. Non-normality quantified by $|\hat{\boldsymbol{\phi}}_1^* \hat{\boldsymbol{\psi}}_1|^{-1}$ agrees well with $\sigma_1 |i\omega - \lambda|$ for both the base and mean flows.

It is important to note that only resonant mechanisms are active in cylinder flow, whereas in more complicated flows such as wall-bounded turbulence, both resonant and pseudoresonant mechanisms are relevant. Three wavenumber triplets, representative of the near-wall cycle, VLSMs, and stationary disturbances, highlight the competing influences of viscous dissipation, mean flow advection, and mean shear on not only the most amplified modes but also the spectrum and pseudospectrum. The importance of each term depends significantly on the wall-normal height where the perturbations are localized. In the inner region where there is very high mean shear and viscosity is most important, amplification is primarily due to pseudoresonant mechanisms. Forcing in the spanwise–wall-normal plane leads to a large response in the streamwise direction as seen for the near-wall cycle mode. The eigenvalues are highly damped yet the resolvent norm is on the order of unity due to the high sensitivity of the spectrum to perturbations. In the logarithmic region, mean shear and consequently lift-up are weaker yet the declining importance of viscosity results in eigenvalues which are closer to the imaginary axis. The most amplified disturbance for wavenumbers corresponding to the VLSM, nevertheless, is primarily due to pseudoresonance. Consequently, there is poor agreement between non-normality quantified by $|\hat{\boldsymbol{\phi}}_1^* \hat{\boldsymbol{\psi}}_1|^{-1}$ and $\sigma_1 |i\omega - \lambda|$ as it is clear that amplification can no longer be attributed to a single eigenvalue. Mean flow advection results in the Orr mechanism (see [33]) and hence less overlap between the forcing and response modes.

Stationary disturbances are the globally most amplified disturbances by effectively leveraging mean shear. The perturbation energy is almost exclusively concentrated in the v and w components of the forcing mode and in the u component of the response mode. Assuming streamwise

constant disturbances eliminates the mean flow advection term from the resolvent operator and hence suppresses the Orr mechanism. All of the non-normality, consequently, can be classified as a component-type non-normality, in contrast to the cylinder flow, and the eigenvalues of the LNS operator are real. Non-normality quantified by $|\hat{\boldsymbol{\phi}}_1^* \hat{\boldsymbol{\psi}}_1|^{-1}$ agrees well with $\sigma_1 |i\omega - \lambda|$ since amplification can be attributed to the eigenvalue closest to the imaginary axis. Finally, the distribution of energy among various velocity components may be useful when considering how the nonlinear term, which can be computed from resolvent response modes [60], projects onto the optimal resolvent forcing modes.

We now lastly discuss the potential application of resolvent-based modal expansions for purposes of reduced-order modeling and control, particularly in relation to the placement of sensors and actuators. The resolvent response modes are outputs which are highly amplified by the linear dynamics of the NSEs, and so sensors could be placed where these are likely to be strong. The resolvent forcing modes are the "trigger" or input which leads to high amplification, and so the actuators could be placed to manipulate the flow in such a way that suppresses these disturbances. In cases where there is large spatial separation between resolvent forcing and response modes, it is possible that improved performance could be attained by sensing and actuating within a wavemaker region (e.g., [31,61]), which, as discussed in Sec. IV, may also be obtained from resolvent analysis. While the resolvent decomposition shows potential for control applications [62], further refinements could seek to balance the observability and controllability of the reduced-order model [63–65], subject to known sensor and actuator locations, and information about the nature of the nonlinear forcing [66].

ACKNOWLEDGMENTS

The work in this study has been financially supported by a National Science Foundation Graduate Fellowship, Air Force Office of Scientific Research (AFOSR), under Grant No. FA 9550-16-1-0361 and Army Research Office (ARO) under Grant No. W911NF-17-1-0306. The authors would like to thank Denis Sipp for providing the resolvent code and Andres Goza who assisted setting it up on a cluster. Finally, the authors would like to acknowledge Theresa Saxton-Fox and Ryan McMullen for useful feedback on the manuscript.

[1] S. E. Turton, L. S. Tuckerman, and D. Barkley, Prediction of frequencies in thermosolutal convection from mean flows, Phys. Rev. E **91**, 043009 (2015).

[2] K. Gudmundsson and T. Colonius, Instability wave models for the near-field fluctuations of turbulent jets, J. Fluid Mech. **689**, 97 (2011).

[3] K. Oberleithner, L. Rukes, and J. Soria, Mean flow stability analysis of oscillating jet experiments, J. Fluid Mech. **757**, 1 (2014).

[4] O. T. Schmidt, A. Towne, T. Colonius, A. V. G. Cavalieri, P. Jordan, and G. A. Brès, Wavepackets and trapped acoustic modes in a turbulent jet: Coherent structure eduction and global stability, J. Fluid Mech. **825**, 1153 (2017).

[5] S. Beneddine, D. Sipp, A. Arnault, J. Dandois, and L. Lesshafft, Conditions for validity of mean flow stability analysis, J. Fluid Mech. **798**, 485 (2016).

[6] D. Barkley, Linear analysis of the cylinder wake mean flow, Europhys. Lett. **75**, 750 (2006).

[7] M. Provansal, C. Mathis, and L. Boyer, Bénard–von Kármán instability: Transient and forced regimes, J. Fluid Mech. **182**, 1 (1987).

[8] K. R. Sreenivasan, P. J. Strykowski, and D. J. Olinger, Hopf bifurcation, Landau equation, and vortex shedding behind circular cylinders, in *Proceedings of the Forum on Unsteady Flow Separation*, edited by K. Ghia (ASME, New York, 1987), Vol. 1, pp. 1–13.

[9] B. R. Noack and H. Eckelmann, A global stability analysis of the steady and periodic cylinder wake, J. Fluid Mech. **270**, 297 (1994).

[10] D. Sipp and A. Lebedev, Global stability of base and mean flows: A general approach and its applications to cylinder and open cavity flows, J. Fluid Mech. **593**, 333 (2007).
[11] V. Mantič-Lugo, C. Arratia, and F. Gallaire, Self-Consistent Mean Flow Description of the Nonlinear Saturation of the Vortex Shedding in the Cylinder Wake, Phys. Rev. Lett. **113**, 084501 (2014).
[12] L. N. Trefethen, A. E. Trefethen, S. C. Reddy, and T. A. Driscoll, Hydrodynamic stability without eigenvalues, Science **261**, 578 (1993).
[13] P. J. Schmid and D. S. Henningson, *Stability and Transition in Shear Flows* (Springer, Berlin, 2001).
[14] M. R. Jovanović and B. Bamieh, Componentwise energy amplification in channel flows, J. Fluid Mech. **534**, 145 (2005).
[15] B. F. Farrell and P. J. Ioannou, Stochastic forcing of the linearized Navier-Stokes equations, Phys. Fluids **5**, 2600 (1993).
[16] K. M. Butler and B. F. Farrell, Three-dimensional optimal perturbations in viscous shear flow, Phys. Fluids A **4**, 1637 (1992).
[17] B. J. McKeon and A. S. Sharma, A critical-layer framework for turbulent pipe flow, J. Fluid Mech. **658**, 336 (2010).
[18] Y. Hwang and C. Cossu, Linear non-normal energy amplification of harmonic and stochastic forcing in the turbulent channel flow, J. Fluid Mech. **664**, 51 (2010).
[19] L. Lu and G. Papadakis, An iterative method for the computation of the response of the linearised Navier-Stokes equations to the harmonic forcing and application to forced cylinder wakes, Int. J. Numer. Methods Fluids **74**, 794 (2014).
[20] J. Jeun, J. W. Nichols, and M. R. Jovanović, Input-output analysis of high-speed axisymmetric isothermal jet noise, Phys. Fluids **28**, 047101 (2016).
[21] O. T. Schmidt, A. Towne, G. Rigas, T. Colonius, and G. A. Brès, Spectral analysis of jet turbulence, arXiv:1711.06296.
[22] S. C. Reddy, P. J. Schmid, and D. S. Henningson, Pseudospectra of the Orr-Sommerfeld operator, SIAM J. Appl. Math. **53**, 15 (1993).
[23] A. E. Trefethen, L. N. Trefethen, and P. J. Schmid, Spectra and pseudospectra for pipe Poiseuille flow, Comput. Methods Appl. Mech. Eng. **175**, 413 (1999).
[24] P. J. Schmid, Nonmodal stability theory, Annu. Rev. Fluid Mech. **39**, 129 (2007).
[25] P. J. Schmid and L. Brandt, Analysis of fluid systems: Stability, receptivity, sensitivity, Appl. Mech. Rev. **66**, 024803 (2014).
[26] J. M. Chomaz, Global instabilities in spatially developing flows: Non-normality and nonlinearity, Annu. Rev. Fluid Mech. **37**, 357 (2005).
[27] U. A. Qadri and P. J. Schmid, Frequency selection mechanisms in the flow of a laminar boundary layer over a shallow cavity, Phys. Rev. Fluids **2**, 013902 (2017).
[28] P. Huerre and M. Rossi, Hydrodynamic instabilities in open flows, in *Hydrodynamics and Nonlinear Instabilities*, edited by C. Godrèche and P. Manneville (Cambridge University Press, Cambridge, UK, 1998).
[29] P. Huerre and P. A. Monkewitz, Absolute and convective instabilities in free shear layers, J. Fluid Mech. **159**, 151 (1985).
[30] P. A. Monkewitz, The absolute and convective nature of instability in two-dimensional wakes at low Reynolds numbers, Phys. Fluids **31**, 999 (1988).
[31] F. Giannetti and P. Luchini, Structural sensitivity of the first instability of the cylinder wake, J. Fluid Mech. **581**, 167 (2007).
[32] D. Sipp, O. Marquet, P. Meliga, and A. Barbagallo, Dynamics and control of global instabilities in open-flows: A linearized approach, Appl. Mech. Rev. **63**, 030801 (2010).
[33] B. J. McKeon, The engine behind (wall) turbulence: Perspectives on scale interactions, J. Fluid Mech. **817**, P1 (2017).
[34] T. Herbert, Parabolized stability equations, Annu. Rev. Fluid Mech. **29**, 245 (1997).
[35] W. C. Reynolds and W. G. Tiederman, Stability of turbulent channel flow, with application to Malkus's theory, J. Fluid Mech. **27**, 253 (1967).

[36] K. Taira, S. L. Brunton, S. T. M. Dawson, C. W. Rowley, T. Colonius, B. J. McKeon, O. T. Schmidt, S. Gordeyev, V. Theofilis, and L. S. Ukeiley, Modal analysis of fluid flows: An overview, AIAA J. **55**, 4013 (2017).
[37] P. Luchini and A. Bottaro, Adjoint equations in stability analysis, Annu. Rev. Fluid Mech. **46**, 493 (2014).
[38] R. Moarref, A. S. Sharma, J. A. Tropp, and B. J. McKeon, Model-based scaling of the streamwise energy density in high-Reynolds-number turbulent channels, J. Fluid Mech. **734**, 275 (2013).
[39] L. Brandt, D. Sipp, J. O. Pralits, and O. Marquet, Effect of base-flow variation in noise amplifiers: The flat-plate boundary layer, J. Fluid Mech. **687**, 503 (2011).
[40] O. Marquet, M. Lombardi, J. M. Chomaz, D. Sipp, and L. Jacquin, Direct and adjoint global modes of a recirculation bubble: Lift-up and convective non-normalities, J. Fluid Mech. **622**, 1 (2009).
[41] M. T. Landahl, A note on an algebraic instability of inviscid parallel shear flows, J. Fluid Mech. **98**, 243 (1980).
[42] W. M. F. Orr, The stability or instability of the steady motions of a perfect liquid and of a viscous liquid. Part II: A viscous liquid, Proc. R. Irish Acad. Sec. A: Math. Phys. Sci. **27**, 69 (1907).
[43] B. F. Farrell, Developing disturbances in shear, J. Atmos. Sci. **44**, 2191 (1987).
[44] P. Meliga, E. Boujo, and F. Gallaire, A self-consistent formulation for the sensitivity analysis of finite-amplitude vortex shedding in the cylinder wake, J. Fluid Mech. **800**, 327 (2016).
[45] M. Juniper, Absolute and convective instability in gas turbine fuel injectors, in *Proceedings of ASME Turbo Expo 2012: Power for Land, Sea and Air, Copenhagen* (ASME, New York, 2012).
[46] I. Gelfand, Zur Theorie der Charaktere der Abelschen topologischen Gruppen, Rec. Math. N. S. **9**, 49 (1941).
[47] L. N. Trefethen and M. Embree, *Spectra and Pseudospectra: The Behavior of Nonnormal Matrices and Operators* (Princeton University Press, Princeton, NJ, 2005).
[48] T. Gebhardt and S. Grossmann, Chaos transition despite linear stability, Phys. Rev. E **50**, 3705 (1994).
[49] D. Barkley and R. D. Henderson, Three-dimensional Floquet stability analysis of the wake of a circular cylinder, J. Fluid Mech. **322**, 215 (1996).
[50] F. Hecht, New development in FREEFEM++, J. Numer. Math. **20**, 251 (2012).
[51] M. Nayar and U. Ortega, Computation of selected eigenvalues of generalized eigenvalue problems, J. Comput. Phys. **108**, 8 (1993).
[52] R. B. Lehoucq and D. C. Sorensen, Deflation techniques for an implicitly restarted Arnoldi iteration, SIAM J. Matrix Anal. Appl. **17**, 789 (1996).
[53] D. Sipp and O. Marquet, Characterization of noise amplifiers with global singular modes: The case of the leading-edge flat-plate boundary layer, Theor. Comput. Fluid Dyn. **27**, 617 (2013).
[54] P. R. Amestoy, I. S. Duff, J.-Y. L'Excellent, and J. Koster, A fully asynchronous multifrontal solver using distributed dynamic shedding, SIAM J. Matrix Anal. Appl. **23**, 15 (2001).
[55] B. J. A. Zielinska, S. Goujon-Durand, J. Dušek, and J. E. Wesfreid, Strongly Nonlinear Effect in Unstable Wakes, Phys. Rev. Lett. **79**, 3893 (1997).
[56] J. A. Weideman and S. C. Reddy, A MATLAB differentiation matrix suite, ACM Trans. Math. Softw. **26**, 465 (2000).
[57] M. J. P. Hack and P. Moin, Algebraic disturbance growth by interaction of Orr and lift-up mechanisms, J. Fluid Mech. **829**, 112 (2017).
[58] J.-L. Bourguignon, Models of turbulent pipe flow, Ph.D. thesis, California Institute of Technology, 2012 (unpublished).
[59] F. Gómez, H. M. Blackburn, M. Rudman, A. S. Sharma, and B. J. McKeon, A reduced-order model of three-dimensional unsteady flow in a cavity based on the resolvent operator, J. Fluid Mech. **798**, R2 (2016).
[60] B. J. McKeon, A. S. Sharma, and I. Jacobi, Experimental manipulation of wall turbulence: A systems approach, Phys. Fluids **25**, 031301 (2013).
[61] K. K. Chen and C. W. Rowley, H_2 optimal actuator and sensor placement in the linearised Ginzburg-Landau system, J. Fluid Mech. **681**, 241 (2011).
[62] M. Luhar, A. S. Sharma, and B. J. McKeon, Opposition control within the resolvent analysis framework, J. Fluid Mech. **749**, 597 (2014).

[63] B. Moore, Principal component analysis in linear systems: Controllability, observability, and model reduction, IEEE Trans. Autom. Control **26**, 17 (1981).
[64] C. W. Rowley, Model reduction for fluids using balanced proper orthogonal decomposition, Int. J. Bifurc. Chaos **15**, 997 (2005).
[65] A. Barbagallo, D. Sipp, and P. J. Schmid, Closed-loop control of an open cavity flow using reduced-order models, J. Fluid Mech. **641**, 1 (2009).
[66] F. Gómez and H. M. Blackburn, Data-driven approach to design of passive flow control strategies, Phys. Rev. Fluids **2**, 021901 (2017).